6

Direct Numerical Simulation of Polymer Electrolyte Fuel Cell Catalyst Layers

Partha P. Mukherjee,[1] Guoqing Wang,[2] and
Chao-Yang Wang[1]*

[1]Electrochemical Engine Center (ECEC), and Department of Mechanical and Nuclear Engineering, The Pennsylvania State University, University Park, PA 16802, USA
[2]Plugpower Inc., 968 Albany-Shaker Road, Latham, NY 12110, USA
** Corresponding Author: e-mail: cxw31@psu.edu, Ph: (814) 863-4762; Fax: (814) 863-4848*

I. INTRODUCTION

Fuel cells, due to their high energy efficiency, zero pollution and low noise, are widely considered as the 21st century energy-conversion devices for mobile, stationary and portable power. Among the several types of fuel cells, polymer electrolyte fuel cell (PEFC) has emerged as the most promising power source for a wide range of applications.

A typical PEFC is schematically shown in Figure 1 and divided into seven subregions: the anode gas channel, anode gas diffusion layer (GDL), anode catalyst layer (CL), ionomeric membrane, cathode CL, cathode GDL, and cathode gas channel. The proton-exchange membrane electrolyte is a distinctive feature of PEFC. Usually the two thin catalyst layers are coated on both sides of the membrane, forming a membrane-electrode assembly

Modern Aspects of Electrochemistry, Number 40, edited by R. White et al., Springer, New York, 2006.

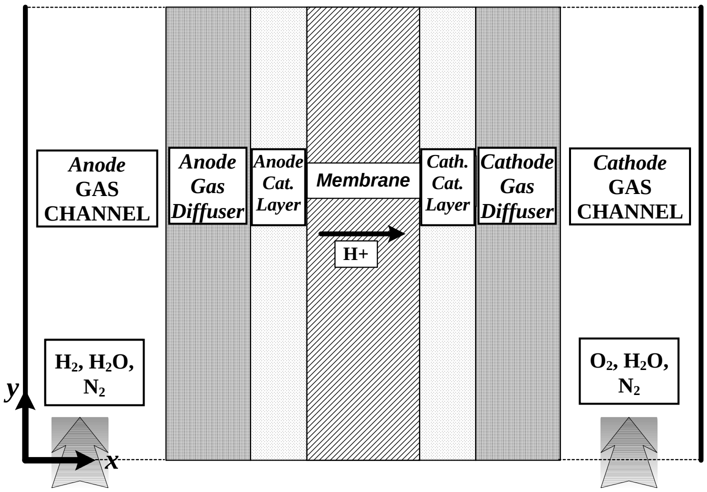

Figure 1. Schematic diagram of a polymer electrolyte fuel cell.

(MEA). The anode feed, generally, consists of hydrogen, water vapor, and nitrogen or hydrogen/water binary gas, whereas humidified air is fed into the cathode. Hydrogen and oxygen combine electrochemically within the active catalyst layers to produce electricity, water and waste heat. The catalyst layer of thickness around 10 μm is, therefore, a critical component of a PEFC and requires extensive treatment. Gottesfeld and Zawodzinski[1] provided a good overview of the catalyst layer structure and functions. The hydrogen oxidation reaction (HOR) occurs at the anode side catalyst layer and protons are generated according to the following reaction:

$$H_2 \rightarrow 2H^+ + 2e^- \tag{1}$$

The oxygen reduction reaction (ORR) takes place at the cathode catalyst layer and water is produced.

$$O_2 + 4H^+ + 4e^- \rightarrow 2H_2O \tag{2}$$

Thus, the overall cell reaction is:

$$2H_2 + O_2 \rightarrow 2H_2O \tag{3}$$

HOR has orders of magnitude higher reaction rate than ORR, which leaves ORR as a potential source of large voltage loss in PEFCs. Due to the acid nature of the polymer membrane and low-temperature operation, Pt or Pt-alloys are the best-known catalysts for PEFCs. For the electrochemical reaction to occur in the cathode catalyst layer, the layer must provide access for oxygen molecules, protons, and electrons. Therefore, the catalyst layer consists of:

1. the ionomer, i.e., the ionic phase which is typically Nafion® to provide a passage for protons to be transported in or out,
2. metal (Pt) catalysts supported on carbon i.e., the electronic phase for electron conduction, and
3. pores for the oxygen gas to be transferred in and product water out. The salient phenomena occurring in the catalyst layer, therefore, include interfacial reaction at the electrochemically active sites, proton transport in the electrolyte, electron conduction in the electronic phase (i.e., Pt/C), and oxygen diffusion through the gas phase, liquid water, and electrolyte phase.

Several modeling approaches have been used for the catalyst layers. In most of the macroscopic models reported in the literature,[2-5] the active catalyst layer was not the main focus but rather treated as a macrohomogeneous porous layer. A few detailed models were specifically developed for PEFC catalyst layers based on the theory of volume averaging and they can be further distinguished as homogeneous model, film model and agglomerate model. Springer and Gottesfeld,[6] Perry et. al.,[7] and Eikerling and Kornyshev[8] presented several analytical and numerical solutions for the cathode catalyst layer under various conditions. Recent reviews by Wang[9] and Weber and Newman[10] provided good overviews of the various catalyst layer models.

However, the above-mentioned macroscopic models do not address localized phenomena at the pore scale. Pisani et al.[11] constructed a pore-level model over an idealized, one-dimensional model geometry of pores and assessed the effects of the catalyst layer pore structure on polarization performance. Recently, a direct numerical simulation (DNS)[12] model has been developed at Penn State Electrochemical Engine Center to describe the oxygen, water and charge transport at the pore level within 2-D and 3-D computer-generated catalyst layer microstructures.

The objective of the current chapter is to present a systematic development of the direct numerical simulation (DNS) model starting with idealized, regular 2-D and 3-D catalyst layer microstructures to a purely random 3-D microstructure and finally to a statistically more rigorous description of a 3-D correlated microstructure. The pore-scale transport of charge and species within a microscopically complex CL microstructure and its importance in the development of high-performance catalyst layers are elucidated.

II. DIRECT NUMERICAL SIMULATION (DNS) APPROACH

As mentioned earlier, traditionally, porous electrodes in fuel cells are modeled using the macrohomogeneous technique, where the properties and variables of each phase are volume-averaged over a representative elementary volume containing a sufficient number of particles.

In such an approach, microscopic details of the pore structure are smeared and the electrode is described using the porosity, interfacial area per unit volume, effective conductivity, diffusivity etc. through a homogenized porous medium. With these volume-averaged variables, macroscopic governing equations are derived from their microscopic counterparts by assuming the uniformity of the microscopic properties within the representative elementary volume, which implies existence of phase equilibrium. In these volume-averaged equations, empirical correlations are used to describe the effective properties as a function of porosity and tortuosity, which are characteristic of the porous structure. Therefore, in the macrohomogeneous model, both the structure and the variables are homogenized microscopically. The effects of the microstructural morphology are ignored and also empirical transport properties need to be introduced. On the microscopic level, however, different modes of oxygen transport are responsible for the reactant supply to the reaction surface in the cathode catalyst layer. The relative importance of each distinct mechanism depends on the specific pore structure and relative volumes of small and large pores. It is also possible that oxygen has to dissolve in and diffuse through the ionomer (i.e., Nafion®) and/or the product liquid water in order to reach the reaction surface. Therefore, using the effective overall diffusion coefficient for oxygen in the porous layer seems to be a gross simplification.

Indeed, a most recent measurement of Stumper et al.[13] indicated that the effective oxygen diffusivity through the composite media of the catalyst layer, microporous layer and gas diffusion layer is only one tenth of its theoretical value in air. A detailed characterization of the pore structure is thus an important prerequisite to describe oxygen transport in a microscopic model. To account for these effects of microphase morphology, a direct numerical simulation (DNS) approach is developed.

The concept of DNS first appeared in the modeling of turbulence in fluid mechanics, where micro-level vortices were traced by solving the Navier-Stokes equations directly, instead of using Reynolds averaging.[14] Another application of DNS is in the study of combustion in porous materials, where the flame thickness is of the same order as the pore size.[15]

The motivation of the DNS modeling is to solve the various point-wise accurate conservation equations on a real microstructure of a porous electrode, instead of the volume-averaged equations based on the homogenized structure. Thus, the geometry of each phase in the porous electrode has to be identified in order to implement the microscopic transport equations for each phase.

1. Advantages and Objectives of the DNS Approach

The advantage of the DNS approach is that the governing equations used are point-wise accurate instead of phase-homogenized equations as in the macrohomogeneous model. Therefore, the DNS model can include the important effects of microstructural morphologies, thus yielding more accurate predictions. In the application to fuel cells, this method can be used to analyze and identify the various losses from the cathode catalyst layer, using computer-generated porous microstructures. Humidity effect of the inlet oxidant can be studied by additionally solving the water transport problem through the catalyst layer. In addition, optimal compositions and structures of various phases in the catalyst layer to achieve minimum voltage loss can be explored using the DNS approach.

Another unique application of the DNS approach is to examine and evaluate the empirical correlations needed in the macrohomogeneous model by building a pore-level database. With the detailed distributions of species concentrations and electrical potentials averaged macroscopically, the effective diffusivity and conductivity can be calculated via Fick’s law and Ohm’s law, respectively. Furthermore, since the macrohomogeneous model is based on the assumptions of homogeneous structures and local equilibrium, the DNS method is the only approach to simulate the thin and highly heterogeneous electrodes (the catalyst layer of 10 μm in thickness is an example), high-rate or fast-transient operations, where the use of a volume-averaging method in a macrohomogeneous model would lose its physical basis.

In addition, the DNS method could distinguish the performance of electrodes when their microstructures vary from each other, and this eventually will help to engineer various micro-morphologies of porous materials for different applications at the phase interfacial scale. However, the DNS model is computationally much more intensive since it resolves the microstructure of a porous electrode. Especially when the real 3D geometries are to be included, it would cost computational time because extremely fine grids would be required to capture each phase intercrossing in a complex manner. Nonetheless, parallel computation on an inexpensive Linux cluster should significantly increase the computing power for DNS calculations.

2. DNS Model - Idealized 2-D Microstructure

There are essentially two steps in the DNS model. The first step is the catalyst layer microstructure reconstruction. The second step is solving transport equations for protons, electrons and chemical species directly on the reconstructed electrode microstructure. For the illustration of these two steps, a two-dimensional regular microstructure is employed first.

An ideal cathode catalyst layer structure would have the following properties: all Pt catalysts should be dispersed on the surfaces between the electronic phase (i.e., carbon) and the electrolyte, typically Nafion®, forming a catalyzed interface for the ORR. This catalyzed interface must be further accessible by oxygen. According to these basic requirements for the catalyst layer, a 2-D cathode catalyst layer is first generated, as shown in Figure 2. In the schematic diagram, *x* direction is along the catalyst layer thickness, and *y* direction represents a periodic repeating unit of a realistic catalyst layer. The physical system includes three phases, an electronic phase, an electrolyte phase and a gas phase. At the interface between the electronic and gas phase, there is a thin electrolyte film, and Pt catalyst is also assumed to exist on the electronic surface so that ORR takes place on this electrochemically catalyzed interface. In the layer, there are ten particles of 2 μm in size arranged along the x direction with a total

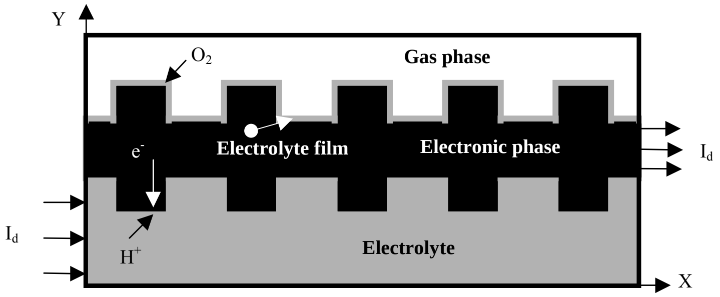

Figure 2. Schematic diagram of the 2-D computational domain.

thickness of 20 μm. The protons migrate through the electrolyte after crossing the membrane located at the left boundary (i.e., $x = 0$) of the domain as explained in Figure 2 and reach the catalyzed interface. At the same time, O_2 diffuses to the catalyst layer from the cathode backing layer at the right boundary (i.e., $x = x_L$) of the domain, and then dissolves in the electrolyte film, where the ORR occurs.

As a first step toward DNS modeling, the following simplifications and assumptions are made:

1. O_2 diffusion resistance through the polymer electrolyte is ignored due to the small thickness of the film (~5 nm). Thermodynamic equilibrium between the gas phase oxygen concentration and that dissolved in the electrolyte phase is assumed to exist at the reaction interface.
2. The product water mass conservation is not considered, assuming that product water is in the gas phase due to heat generation in the CL and diffuses out of CL sufficiently fast. This assumption may bring considerable error at large current densities, which will be justified later.
3. The proton conductivity in the polymer electrolyte is treated as constant, though it actually depends on the water content in the ionomer. This assumption will be relaxed in Section IV.
4. The cell operation temperature is assumed to be constant and steady state is assumed.

A single set of differential equations valid for all the phases is developed, which obviates the specification of internal boundary conditions at the phase interfaces. The mass balance of O_2, charge conservation and the electrochemical reaction are formulated based on the above assumptions. Due to slow kinetics of the ORR, the electrochemical reaction is assumed to be governed by Tafel kinetics as follows:

$$j = -i_0 \frac{c_{O2}}{c_{O2,ref}} \exp\left(\frac{-\alpha_c F}{RT} \eta \right) \tag{4}$$

where, i_0 is the exchange current density, c_{O2} and $c_{O2,ref}$ refer to local oxygen concentration and reference oxygen concentration respectively, α_c is the cathode transfer coefficient for ORR, F is the Faraday's constant, R is the universal gas constant, and T is the cell operating temperature. The overpotential, η, is defined as:

$$\eta = \phi_s - \phi_e - U_o \tag{5}$$

where, ϕ_s and ϕ_e are the electronic and electrolyte phase potentials at the reaction site respectively. U_o is the thermodynamic equilibrium potential of the cathode under the cell operation temperature.

The charge conservation for electron and proton and O_2 conservation can be described by the following equations, respectively:

$$\nabla \cdot \left(\sigma \nabla \phi_s \right) + a \int_\Gamma j \delta(x - x_{\text{int erface}}) ds = 0 \tag{6}$$

$$\nabla \cdot \left(\kappa \nabla \phi_e \right) + a \int_\Gamma j \delta(x - x_{\text{int erface}}) ds = 0 \tag{7}$$

$$\nabla \cdot \left(D \nabla c_{O2} \right) + a \int_\Gamma \frac{j}{4F} \delta(x - x_{\text{int erface}}) ds = 0 \tag{8}$$

where, a represents the specific interfacial area and is defined as the interfacial surface area where the reaction occurs per unit volume of the catalyst layer, s is the interface, Γ represents the interfacial surface over which the surface integral is taken, $\delta(x - x_{\text{interface}})$ is a delta function which is zero everywhere but unity at the interface where the reaction occurs. The transfer current, j, is positive for the electronic phase and negative for the electrolyte since the current is transferred from the electronic phase into the electrolyte. σ and κ represent electronic conductivity and electrolyte conductivity respectively and D refers to the oxygen diffusivity in the gas phase.

At the left boundary, a constant current density, i_d, is applied through the electrolyte phase, while it flows out from the electronic phase on the right boundary. A constant value of oxygen concentration, c_{O_2} , equal to the gas channel inlet value, $c_{O_2,0}$, is assumed at the right boundary. The boundary conditions can then be expressed as:

$$c_{O_2} = c_{O_2,0} \qquad \text{in the gas phase at } x=x_L, \tag{9}$$

$$-\kappa \frac{\partial \phi_e}{\partial x} = i_d \qquad \text{in the electrolyte phase at } x = 0, \tag{10}$$

$$-\sigma \frac{\partial \phi_s}{\partial x} = i_d \qquad \text{in the electronic phase at } x = x_L, \tag{11}$$

and,

$$\frac{\partial c_{O_2}}{\partial n} = 0 \ , \ \frac{\partial \phi}{\partial n} = 0 \quad \text{everywhere for other boundaries} \tag{12}$$

The governing equations are discretized by the control-volume-based finite difference method by Patankar,[16] and the resulting sets of algebraic equations are iteratively solved. The rectangular physical domain is divided into uniform grids. The numerical grids used in the following simulations are 160 in the x direction and 24 in the y direction. All the parameters, including the properties of each phase, are given in Table 1. The equations are solved simultaneously, and convergence is considered to be reached when the relative error in each field between two consecutive iterations is less than 10^{-5}.

3. Three-Dimensional Regular Microstructure

The idealized two-dimensional CL microstructure is bound to show some departure from reality. For instance, the reaction area obviously seems to be much less than that in a real 3-D catalyst layer, in which case the reaction area is roughly 100-times larger than the nominal electrode cross-sectional area. However, the main purpose of the 2-D DNS model is to demonstrate the concept and

Table 1
Property Data for the DNS Calculations with the Regular 2-D and 3-D Microstructure

Parameter	Solid phase	Electrolyte	Gas phase
Conductivity, σ (S/cm)	50	0.05	0
O_2 diffusion coefficient, $D^{g}_{O_2,0}$ (cm^2/s)	0	0	0.01
Pressure at the gas channel inlet, p (kPa)	150		
Reference concentration, (mol/cm^3)	51.1×10^{-6}		
Temperature, T (°C)	80		
Catalyst layer thickness, (μm)	20		
Simulation height of layer, (μm)	3		
Volume fraction of electronic phase, ε_s	0.5		
Volume fraction of electrolyte, ε_e	0.25		
Volume fraction of gas phase, ε_g	0.25		
Exchange current density, i_0 (A/cm^2)	1.0×10^{-8}		
Cathodic transfer coefficient, α_c	1.0		
Open-circuit potential, U_0 (V)	1.1		

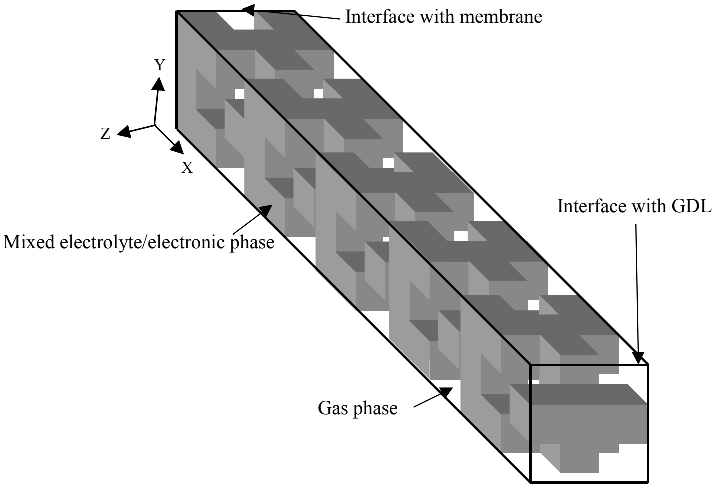

Figure 3. Schematic diagram of the 3-D regular microstructure.

utility of the DNS approach in assessing the effects of the micro-morphology on diffusion and reaction. This model also allows for a fundamental understanding of the physics occurring in the catalyst layer.

As an attempt toward describing a more realistic CL microstructure, the DNS model is now extended to a three dimensional CL microstructure, as shown in Figure 3. Here, the catalyst layer is simplified to contain two phases, the gas phase and a mixed electrolyte/electronic phase. On the left boundary, the protons migrate into the catalyst layer from the membrane. Oxygen and electrons reach the CL through the gas voids and electronic phase, respectively, at the right boundary, attached to the GDL. A typical CL is about 10–20 μm in thickness and the pore size is about one to two order of magnitude smaller. In the *y-z* directions, the computational domain is assumed to have symmetry boundary conditions such that many repeating units constitute the entire catalyst layer.

A few assumptions are additionally made to the regular three-dimensional catalyst layer structure for simplicity.

- The electronic phase potential is assumed to be uniform because the electrode is very thin and its electronic conductivity is sufficiently high. Under this assumption, the mixed phase is treated as an electrolyte phase by applying an effective ionic conductivity. This correction accounts for the volume fraction of the electrolyte phase with respect to the mixed phase volume fraction and thus assumes a Bruggeman type correlation as:

  $$\kappa = \kappa_0 \cdot (\frac{\varepsilon_e}{\varepsilon_e + \varepsilon_s})^{1.5} = \kappa_0 \cdot (\frac{\varepsilon_e}{1-\varepsilon_g})^{1.5} \qquad (13)$$

  where, κ_0 is the intrinsic conductivity of the electrolyte, ε_e, ε_s and ε_g are the electrolyte, electronic and gas pore volume fractions, respectively. For simplicity, the mixed electrolyte/electronic phase will be referred to simply as the electrolyte phase in the rest of the chapter.
- The interface between the gas phase and the mixed phase is assumed to be completely catalyzed and activated by platinum nanoparticles. Therefore, the entire interface is active for the ORR.
- The system is also assumed to be isothermal and steady state is considered.

Under the aforementioned assumptions, the governing equations for charge and oxygen conservation can be written, respectively, as:

$$\nabla \cdot (\kappa \nabla \phi_e) + a \int_{\Gamma} j \delta(x - x_{\text{interface}}) ds = 0 \tag{14}$$

$$\nabla \cdot (D^g_{O_2} \nabla c_{O_2}) + a \int_{\Gamma} \frac{j}{4F} \delta(x - x_{\text{interface}}) ds = 0 \tag{15}$$

The second term in both the equations represents a source/sink term only at the catalyzed phase interface where the electrochemical reaction takes place.

In order to facilitate numerical solution of Eqs. (14) and (15) without having to resolve the microscopically complex phase interface, the governing equations are extended to the entire computational domain by incorporating a phase function *f*. The phase function is defined as unity in the electrolyte phase and zero in the gas phase, respectively. The proton conductivity and oxygen diffusivity can be generally expressed, at each cell center, in terms of the discrete phase function as:

$$K(i,j,k) = \kappa \cdot f(i,j,k) \tag{16}$$

$$D(i,j,k) = D^g_{O_2} [1 - f(i,j,k)] \tag{17}$$

The transfer current between the two neighboring cells at the phase interface, shown in Figure 4, is given by the Tafel equation as follows:

$$j = i_0 \frac{c_{O_2}(i+1,j,k)}{c^{O_2}_{g,ref}} \exp[\frac{\alpha_c F}{RT} \phi_e(i,j,k)] \ (\text{A/cm}^2) \tag{18}$$

$\phi_e(i,j,k)$ is used to represent the overpotential in the kinetic expression since both the open-circuit potential and the electronic phase potential are constant. It is worth noting that the prefactor, i_0, is the modified exchange current density after replacing overpotential, η, in Eq. (4) with the expression given by Eq. (5). The control volume, with cell center (*i,j,k*), forms six interfaces with the neighbors where the electrochemical reaction might occur.

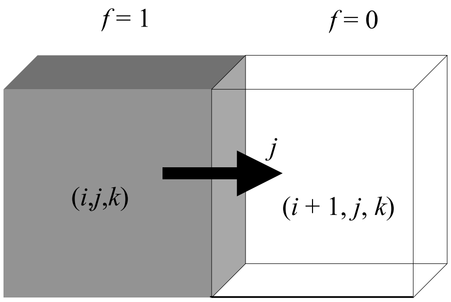

Figure 4. Transfer current between the two adjacent cells.

The sum of the flux from all the reactions can be expressed as the volumetric source term. The corresponding source terms, S_ϕ and S_{O_2} , in the governing equations, Eqs. (14) and (15), respectively, can be expressed in a discretized fashion at the cell center (*i, j, k*) as:

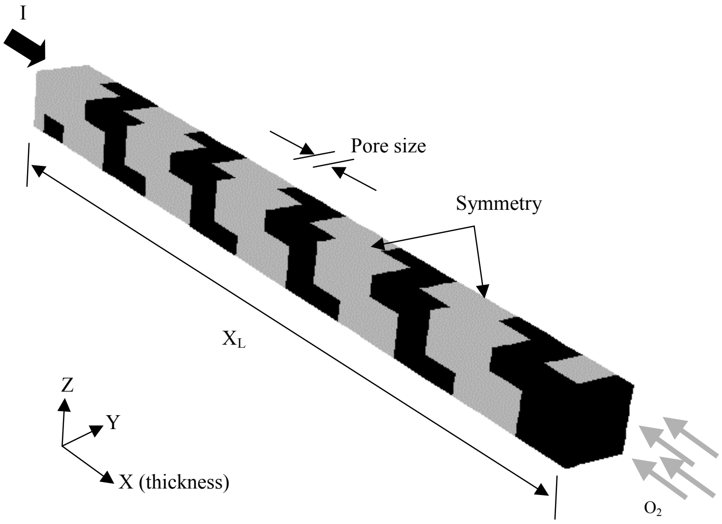

Figure 5. Computational domain for the 3-D DNS model.

$$\begin{aligned}
S_{\phi}(i,j,k) = -\frac{i_0}{c^{g}_{O_2,ref}} f(i,j,k)\exp[\frac{\alpha_c F}{RT}\phi_e(i,j,k)]\cdot \\
\{[1-f(i-1,j,k)]c_{O_2}(i-1,j,k)/\Delta x \\
+[1-f(i+1,j,k)]c_{O_2}(i+1,j,k)/\Delta x \\
+[1-f(i,j-1,k)]c_{O_2}(i,j-1,k)/\Delta y \\
+[1-f(i,j+1,k)]c_{O_2}(i,j+1,k)/\Delta y \\
+[1-f(i,j,k-1)]c_{O_2}(i,j,k-1)/\Delta z \\
+[1-f(i,j,k+1)]c_{O_2}(i,j,k+1)/\Delta z\}
\end{aligned} \tag{19}$$

$$\begin{aligned}
S_{O_2}(i,j,k) = -\frac{i_0}{4Fc^{g}_{O_2,ref}}[1-f(i,j,k)]c_{O_2}(i,j,k)\cdot \\
\{f(i-1,j,k)\exp[\frac{\alpha_c F}{RT}\phi_e(i-1,j,k)]/\Delta x \\
+f(i+1,j,k)\exp[\frac{\alpha_c F}{RT}\phi_e(i+1,j,k)]/\Delta x \\
+f(i,j-1,k)\exp[\frac{\alpha_c F}{RT}\phi_e(i,j-1,k)]/\Delta y \\
+f(i,j+1,k)\exp[\frac{\alpha_c F}{RT}\phi_e(i,j+1,k)]/\Delta y \\
+f(i,j,k-1)\exp[\frac{\alpha_c F}{RT}\phi_e(i,j,k-1)]/\Delta z \\
+f(i,j,k+1)\exp[\frac{\alpha_c F}{RT}\phi_e(i,j,k+1)]/\Delta z\}
\end{aligned} \tag{20}$$

From Eq. (19), it is evident that only the electrolyte phase, with neighboring gas phase cells, has a non-zero source term for charge transport. Likewise, Eq. (19) defines non-zero source term due to oxygen consumption only for that gas phase cell having neighboring electrolyte cells.

The computational domain, as schematically shown in Figure 5, is taken as one quarter of the whole domain, shown in Figure 3, due to symmetry considerations in the *y* and *z* directions. The domain size is 20 μm × 3 μm × 3 μm. At the left boundary, through which the protons migrate from the membrane, one layer of electrolyte-only cells is added to the computational domain. The operating current is uniformly applied on this additional layer, making the boundary condition straightforward to be implemented. For the same purpose, one layer of pore-only cells is applied at the right boundary, which supplies oxygen at a constant concentration. The boundary conditions can be summarized as:

- on the symmetry planes:

$$y = 0\,, y = y_L\,,\ z = 0\,,\ z = z_L\,, \qquad \frac{\partial c_{O_2}}{\partial n} = 0\ ,\ \frac{\partial \phi_e}{\partial n} = 0 \qquad (21)$$

- at the left boundary (i.e., CL-membrane interface):

$$x = 0\,, \qquad \frac{\partial c_{O_2}}{\partial n} = 0\ ,\ -\kappa \frac{\partial \phi_e}{\partial n} = i_d \qquad (22)$$

- at the right boundary (i.e., CL-GDL interface):

$$x = x_L\,, \qquad c_{O_2} = c_{O_2,0}\ ,\ \frac{\partial \phi_e}{\partial n} = 0 \qquad (23)$$

The transport properties and the electrochemical kinetic parameters used in this three-dimensional study are mainly taken from Table 1 in order to compare the results with those from the two-dimensional predictions.

A baseline simulation, with nominal porosity of 0.25 and with uniform mesh size of 42x12x12 in the *x*, *y* and *z* directions, respectively, was performed.

4. Results and Discussion

(*i*) *2-D Model: Kinetics- vs. Transport-Limited Regimes*

In this section, the capabilities of the present model are illustrated by comparing the simulation results with some experimental data. Further, the simulation results are analyzed to understand the various voltage losses from the cathode catalyst layer during its operation. Two sets of simulations are carried out using pure oxygen and air as oxidants at various current densities. Oxygen and air are both fed at a pressure of 150 kPa when the cell is operated at 80 °C. In each set of simulations, a special case, in which the diffusion coefficient of O_2 in the gas phase is set to be infinitely large, is simulated to mimic the limiting case without O_2 depletion effect. Then the two groups of results are compared with corresponding experimental measurements from the literature, under similar conditions.

Polarization curves for various simulations are summarized in Figure 6, including an analytical solution for the limiting case with both infinitely large proton conductivity in the electrolyte and O_2 diffusivity in the gas phase. In general, when the conductivities of both electronic phase and electrolyte phase become infinitely large, the overpotential will be uniform across the electrode with a constant open-circuit potential. Then if the mass diffusivity of the reactant is set to infinitely large to have a uniform concentration distribution, the electrochemical reaction rate will be uniform throughout the electrode. In this case with Tafel kinetics, the current balance for the catalyst layer can be written as follows:

$$i_0 \frac{c_{O_2}}{c_{O_2,ref}} \exp(-\frac{\alpha_c F}{RT}\eta).A_{reaction} = i_d .A_{cross} \tag{24}$$

where $A_{reaction}$ stands for the total reaction area, and A_{cross} represents the cross-sectional area on which the discharge current density i_d is

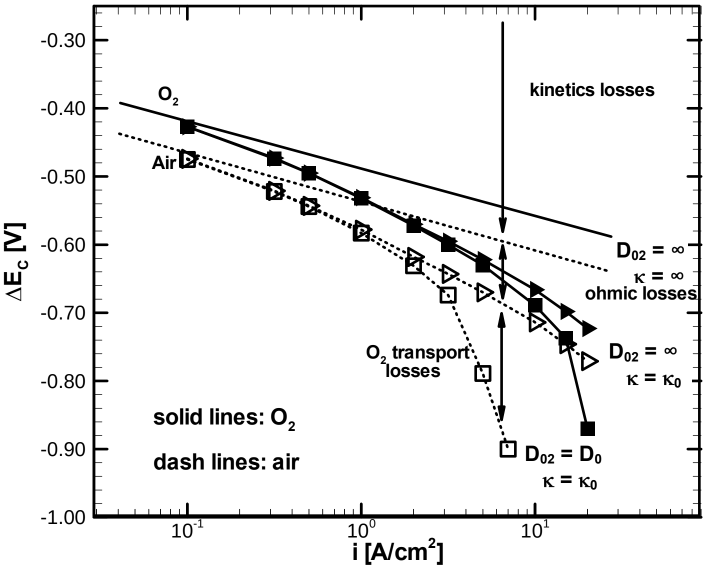

Figure 6. Numerical predictions of the voltage losses in the cathode catalyst layer.

applied. It should be noted that the concentration, c_{O_2} and overpotential, η, are constant in Eq. (24). A new parameter is defined to denote the area ratio, which is given by:

$$A_0 = \frac{A_{reaction}}{A_{cross}} \tag{25}$$

The only voltage loss in this case is the kinetics loss, which can be derived as:

$$|\eta| = 2.303\frac{RT}{\alpha_c F}[\log i_d - \log(A_0 i_0 \frac{c_{O_2}}{c_{O_2,ref}})] \tag{26}$$

In Eq. (26), the coefficient at the right hand side,$2.303RT/\alpha_c F$, is the Tafel slope, denoted as b and having the unit of mV/dec. In our simulation, b has the value of 70 mV/dec with α_c of 1.0 and an operating temperature of 80 °C. Eq. (26) states that in the absence of ohmic and transport losses, the cathode voltage drop will increase by 70 mV once the current density i_d increases by a factor of 10 or the concentration, c_{O_2} , the area ratio A_0 decrease by a factor of 10. In Figure 6, the two straight lines show the pure kinetics losses for O_2 and air as oxidant, respectively. Since the mole fraction of O_2 in air is 0.21, there will be about 47 mV more losses when air is used instead of pure O_2 from the following calculation:

$$\Delta E_{O_2 \Rightarrow air} = 70 \cdot \log\left(\frac{100\%}{21\%}\right) = 47mV \tag{27}$$

Figure 6 also indicates that there are additional voltage losses when real electrolyte conductivity and O_2 diffusivity are employed. These additional losses have been identified as ohmic losses and O_2 transport losses in the plot. To reveal these losses, the distributions of O_2 concentration and overpotential are plotted for three different cases in Figure 7. The corresponding operating current density is 3.16 A/cm^2 with air as the oxidant. When realistic electrolyte conductivity is used, the overpotential becomes non-uniform as shown by the dash line. The overpotential at the interface with the membrane, η_0, which represents the total voltage loss at the catalyst layer, increases significantly from the dash dot

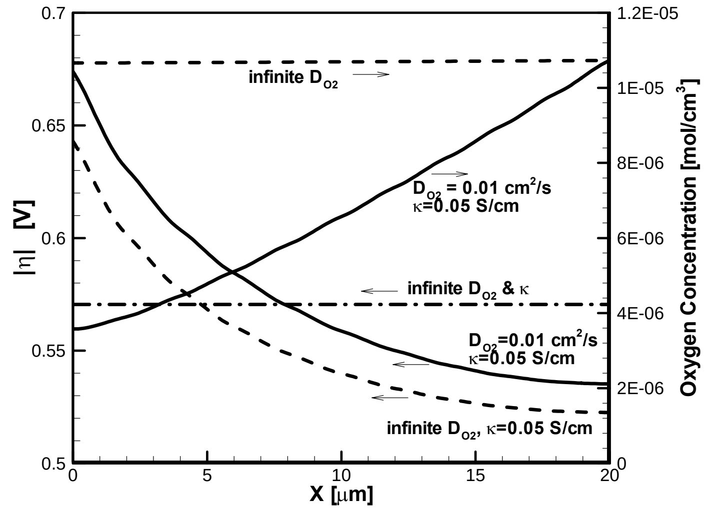

Figure 7. Distributions of the overpotential and oxygen concentration across the thickness of the catalyst layer at current density of 3.16 A/cm^2.

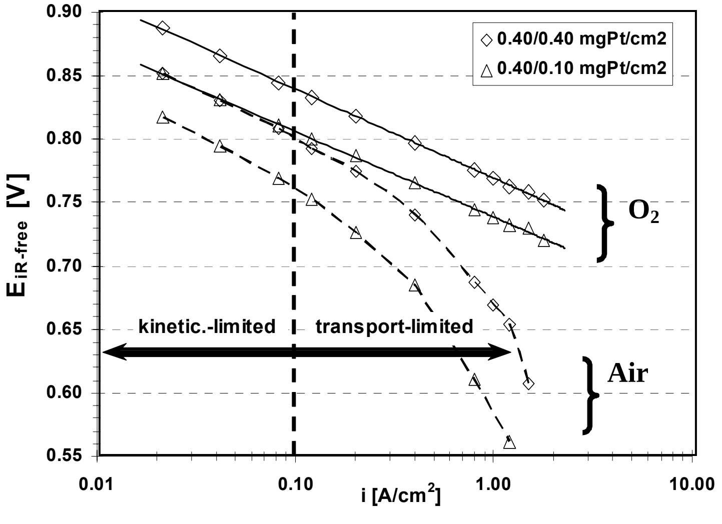

Figure 8. Experimental observations of the voltage losses (Gasteiger *et al.*[17]).

line to the dash line, when κ changes from infinity to 0.05 S/cm. When realistic diffusivity is incorporated, as shown by the solid line, η_0 becomes even larger due to the O_2 diffusion resistance. The value of η_0 could increase further if O_2 is depleted at the CL-GDL interface, which would occur at a higher current density. Correspondingly, these two additional voltage losses are marked as ohmic losses and O_2 transport losses in Figure 6.

Experimental data by Gasteiger et al.[17] is plotted in Figure 8 in a similar fashion as in Figure 6. The *y*-axis denotes the cathode IR-free potential by eliminating all ohmic resistances. Different Pt loadings are applied for both O_2 and air as oxidants. It is observed that the curves simply shift down when the lower Pt-loading of 0.10 mg Pt/cm^2 is applied at the cathode. This is because the total reaction area has decreased, subsequently increasing the kinetics losses, as explained by Eq. (26).

Now, comparing the numerical results in Figure 6 with the experimental observations, in Figure 8, reveal that the kinetic losses look different quantitatively. At the current density of 0.1 A/cm^2, the ORR kinetics losses in the experiments are about 370 mV with an equilibrium potential of 1.18V corresponding to the air oxidant and 0.40 mg Pt/cm^2 catalyst loading in cathode. However, the same losses in the numerical simulation are as large as 470mV. This difference is mainly due to the small reaction surface area in the idealized structure used in the simulations. It can be estimated that the total surface area ratio of Pt catalyst at the cathode is about 140 cm^2 Pt/cm^2 (electrode cross-sectional area) in experiments when 0.40/0.40 mg Pt/cm^2 Pt loadings are used with typical dispersion surface area of Pt particles at 35 m^2/g Pt. On the other hand, this value in the model is only 10. Consequently, this difference by an order of magnitude in the surface area results in more voltage losses by as much as 80mV in simulations than that in experiments. Furthermore, the Tafel slope obtained from the experiments is measured to be 66mV/dec, while being 70 mV/dec in simulations. This leads to another 30 mV more kinetics losses in the simulation results than the experimental data.

Secondly, the O_2 transport characteristics appear different between experiments and simulations, though they are in qualitative agreement. In Figure 8, the transport-limited regime is identified when the current density is larger than 0.1 A/cm^2, which means the transport losses begin to appear in that region for air oxidant. In simulations, when air is used as oxidant, the transport of O_2 does not result in additional voltage drop until the current density is increased to 1 A/cm^2, where the two dash lines begin to deviate from each other. For pure oxygen as the oxidant, the diffusion becomes limiting at 5 A/cm^2, although the experiments have not been carried out at such a high rate. There are three factors that could explain why the O_2 transport losses appear later in the simulations than in the experiments. The most important reason is perhaps due to very high diffusion through the idealized geometry of pore spaces, as mentioned earlier. Furthermore, in the present model, the blocking effect of product water has not been considered, which could also help O_2 diffusion to some extent. Another possible explanation is that at the interface between the simulated catalyst layer and the gas diffusion layer (GDL), the O_2 concentration value is assumed to be the same as that at the inlet of the flow channel. Neglecting the diffusion resistance through the GDL could make the concentration, c_{O_2} , on the right boundary significantly larger than the realistic value.

(*ii*) *Comparison of the Polarization Curves between 2-D and 3-D Simulations*

The polarization curve from the three-dimensional DNS calculation is compared in Figure 9 together with that from the two-dimensional results. These two simulations are carried out under exactly the same conditions, except for the different geometries. It should be noted that the term "polarization curve" refers to the voltage loss vs. current density curve throughout this chapter instead of the standard I-V curve, otherwise used widely in the fuel cell literature. As expected, the effects brought by the three-dimensional geometry can be identified in two different regimes. In the kinetic control regime, voltage loss from the three-dimensional model is about 20 mV less than that for the two dimensional model. Apparently this is due to the increased phase interfacial area, which is one of the purposes to introduce the three-dimensional model. From the calculation, the total interfacial area for the 3-D geometry is around 20 times the electrode cross-sectional area, doubling the total area from the 2-D geometry. Therefore, it results in 20 mV less kinetics losses based on the 70 mV/dec Tafel slope as calculated in Eq. (26). Another influence of the 3-D geometry is reflected on the transport of oxygen. Due to more tortuous path of the 3-D structure, oxygen transport through the gas phase is restricted in the 3-D geometry. As a result, oxygen depletion occurs earlier and the mass transport limiting current density decreases.

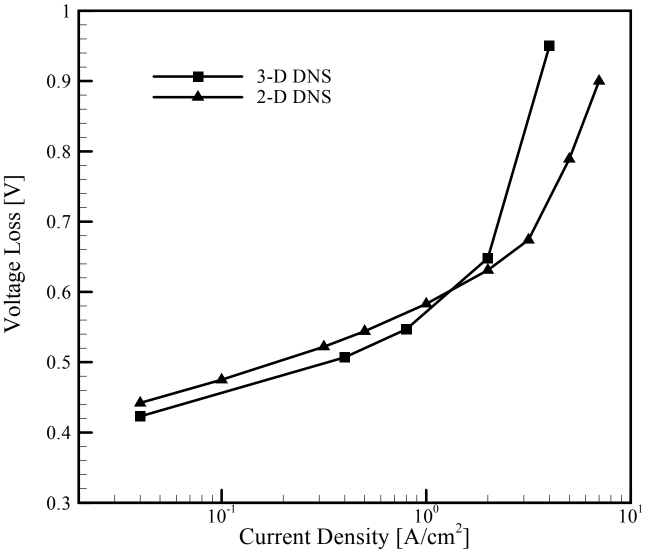

Figure 9. Comparison of the polarization curves from the 2-D and 3-D DNS calculations.

From the above discussions, it is evident that the DNS approach has been successfully deployed to delineate the various physical processes accounting for the different voltage losses in the cathode catalyst layer. The comparison with experimental results further points to several areas of improvements, which include a better representation of the morphology of the porous microstructure and the consideration of water distribution. These issues are addressed in the subsequent sections.

III. THREE-DIMENSIONAL RANDOM MICROSTRUCTURE

In Section II, a regular microstructure was constructed to represent the simplified three-dimensional cathode catalyst layer for application of the DNS model. The regular 3-D structure, while offering an improvement over the two-dimensional geometrical simplicity, is still plagued with morphological and associated physical limitations. Besides the simplicity of the structure, statistical information still deviates from a realistic porous catalyst layer. For example, the phase interfacial area in the simplified structure needs further enhancement and the constituent phases are not as tortuous as that in a practical porous medium, as well. In this section, a purely random porous microstructure is constructed and the 3-D DNS model is extended accordingly.

The general objective of constructing a random microstructure is to mimic more closely the geometry of a real porous medium so as to preserve its statistical feature. This method is able to generate "digital" microstructures with desired properties. As a general approach, certain low-order statistical properties (e.g., porosity and two-point correlation function) of the real porous medium are measured experimentally first and an artificial medium is reconstructed with the same average parameters.

1. Random Structure

Except for a few man-made microstructures, most of the real porous media are random. However, the word 'random' is quite vague and it can be used to qualify very different situations, such as pure disorder and correlated disorder in a porous medium and thus requires more precise definition.

For an arbitrary piece of porous medium, the pore structure can be completely characterized by a binary phase function, $Z(\vec{r})$, which assumes discrete values in the 3-D space as:[18]

$$Z(\vec{r}) = \begin{cases} 1 & \text{if } \vec{r} \text{ is in the pore space} \\ 0 & \text{otherwise} \end{cases} \tag{28}$$

where, $\vec{r}$ denotes the position with respect to an arbitrary origin. The first two moments of the phase function, the porosity, ε, and the autocorrelation function, $R_Z(\vec{u})$, are defined respectively as:[18]

$$\varepsilon = \overline{Z}(\vec{r}) \tag{29}$$

$$R_Z(\vec{u}) = \overline{[Z(\vec{r}) - \varepsilon][Z(\vec{r}+\vec{u}) - \varepsilon]} / (\varepsilon - \varepsilon^2) \tag{30}$$

where, overbar denotes statistical averages. Porosity, ε, is a positive quantity limited to [0, 1] interval and is the probability that a point is in the pore space. $R_Z(\vec{u})$ verifies the general properties of a correlation function and is the probability that two points in the porous medium at a distance, $\vec{r}$, are both in the pore space. For a statistically homogeneous porous medium, ε is a constant and $R_Z(\vec{u})$ is only a function of the lag vector, $\vec{u}$, and does not depend on the spatial coordinates (i.e., independent of $\vec{r}$). Additionally, if the medium is isotropic, then the autocorrelation function does not depend on the direction but only on the norm, u, of the vector, $\vec{u}$. Furthermore, for a purely disordered porous medium, the autocorrelation function is independent of u and identically goes to zero. In such a porous structure, each elementary space, resulting from the discretization of the 3-D continuum space, is occupied at random either with solid or void with a given probability, ε and can be realized, in principle, by throwing a dice. This simplest construction rule is used here to generate a purely random 3-D catalyst layer microstructure for the DNS model.

In the present work, a purely random porous medium is computer-generated by employing a random number generator with porosity, ε and pore size, d as the chosen target geometry features for the reconstruction to match. Specifically, the porous catalyst layer is constructed in a discrete manner. It is considered to be composed of $N_x \times N_y \times N_z$ elementary cubes, each of the same size d, which represents the chosen pore scale. These elementary cubes are filled with either the electrolyte phase or pore phase. During construction, the computer generates a random number uniformly distributed within the interval [0, 1] for each cube. When the random number is lower than the given porosity, ε, the corresponding cube is set to be occupied by the pore space. Otherwise, it is occupied by the electrolyte phase.

2. Structural Analysis and Identification

Once the microstructure is constructed, structural connectivity needs to be imposed by forming pore clusters consisting of a group of connected pores. From structural viewpoint, a group of pores, which are connected with each other, is called a pore cluster. When ε is small, all the pores form small and isolated clusters. When ε is large enough, among all the pore clusters, there would be one that penetrates the entire medium from one end to the other. This kind of pore cluster can be termed as “transport” pore cluster, because it forms a continuous network allowing the fluid to transport across the entire medium. In other words, the porous medium is permeable only if such a “transport” pore cluster exists. A pore belonging to the “transport” pore cluster is called a “transport” pore, otherwise it is called a “dead” pore. Apparently, when ε increases, there would be fewer and fewer “dead” pores. When ε is close to one, all the pores would be “transport” pores.

In the current work, the constructed random cathode catalyst layer structure is depicted in Figure 10. The elementary cube size is 0.25 μm, representing the chosen pore size. Therefore, to simulate the 10 μm-thick catalyst layer, 40 cubes are applied along the thickness. Similar to the approach adopted in the 3-D regular structure, as described in the earlier section, one layer of electrolyte-only and pore-only cells are added to the left and right boundaries of the structure, respectively, for ease of implementation of the boundary conditions.

The numerical approach of identifying the “transport” and “dead” portions for each phase starts with assigning an initial value of a phase function, f, to each elementary control volume in the entire computational domain. On the left boundary of electrolyte-only cells, f is set to be one; while f is assigned to be zero within the pore-only cells on the right boundary. Elsewhere within the

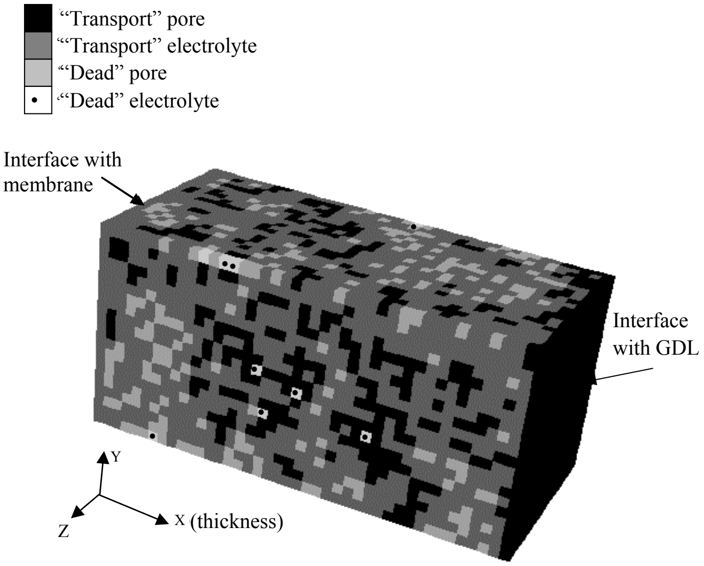

Figure 10. Schematic diagram of the 3-D random catalyst layer microstructure with nominal porosity of 0.36.

domain, *f* is three inside the electrolyte cells and two inside the pore cells. Then beginning from the left boundary, each elementary cell is scanned to identify the “transport” electrolyte. For the cell with *f* equal to three, if any of its six neighboring cells has *f* equal to 1, the phase function *f* of itself is switched to 1. After each scan of the entire domain, the total number of cells with *f* equal to three is counted. This scan form left to right is repeated until the total number does not vary anymore. Thus cells with *f* equal to one are identified as “transport” electrolyte, while those with *f* equal to three represent “dead” electrolyte. Similarly for the pore phase, the scanning process begins from the right boundary to the left and once a cell with *f* equal to two has any neighboring cell with *f* equal to zero, the phase function *f* the cell itself is switched to zero. After sufficient number of scans, when the total number of cells with *f* equal to two does not change anymore, the cells with *f* equal to zero and two are identified as “transport” and “dead” pores, respectively.

The “transport” pore and the “transport” electrolyte identified here represent those elementary cells which are accessible for oxygen from the gas diffusion layer (GDL) at the right boundary

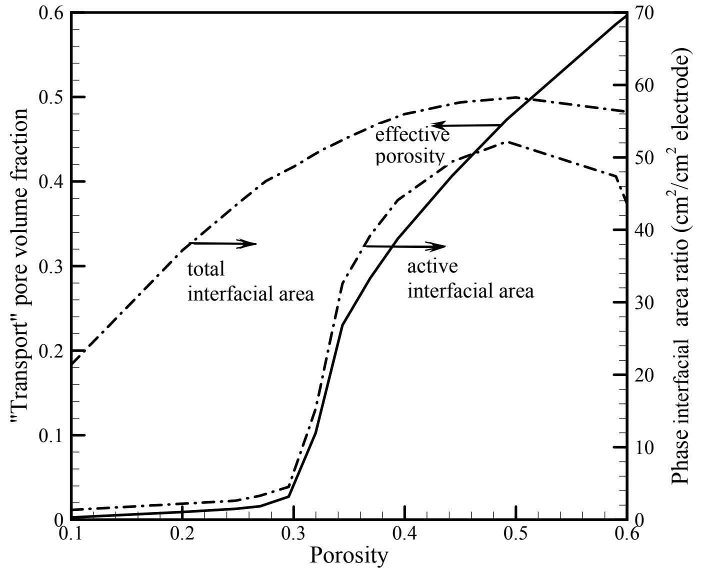

Figure 11. Variation of transport pore volume fraction and phase interfacial area ratio with nominal porosity.

and the protons from the polymer electrolyte membrane at the left boundary, respectively. In Figure 10, the identified "transport" pore and electrolyte cells, as well as "dead" pore and electrolyte cells are indicated with different gray cubes, corresponding to a natural porosity of 0.36. As expected, there are few "dead" electrolyte cells since the electrolyte volume fraction is relatively large (0.64). On the other hand, only about 70% of total pores are identified as "transport" pores, indicating the effective "transport" porosity is only about 0.26.

Figure 11 shows the effective porosity and phase interfacial area ratio as a function of the natural porosity. The phase interfacial area ratio represents the ratio of the interfacial area in a porous structure to the cross-sectional geometrical area. Here, the total interfacial area ratio represents all interfaces between the electrolyte and pore phases, while the active interfacial area ratio only includes those between "transport" electrolyte and "transport" pores, indicating that the interfacial sites are accessible by protons, electrons and oxygen and hence cause the electrochemical reaction to happen. The figure only shows the natural porosity range up to 0.6 because the effective porosity is nearly identical to the natural porosity when it is larger than 0.6. The interfacial area ratio curve is symmetric around the porosity of 0.5. It is also observed that when the porosity is smaller than 0.35, both effective porosity and active interfacial area ratio are reduced dramatically. This is of significance in practical applications, indicating that 0.35 is the low end of the porosity for the catalyst layer. Furthermore, the random microstructure provides a realistic active interfacial area ratio between 40 and 50. This value of the reaction area ratio corresponds roughly to 0.15 mg Pt/cm^2 catalyst loading with a typical dispersion surface area of 35 m^2/g Pt, which is representative in current applications.

The local profiles of pore and electrolyte volume fractions along the thickness of the catalyst layer are shown in Figure 12. First, the cross-section averaged local natural porosity shows a random fluctuation around the average porosity of the porous structure marked by the horizontal line. Secondly, almost all the electrolyte cells are available for transport, while a considerable portion of the pores are dead pockets. The percentage of "transport" pores, distributes uniformly in most locations except for the front and back end of the structure. At the back end (i.e., near the left boundary) of the catalyst layer, interfacing with the membrane, more pores are "dead" indicating difficulty in access for the

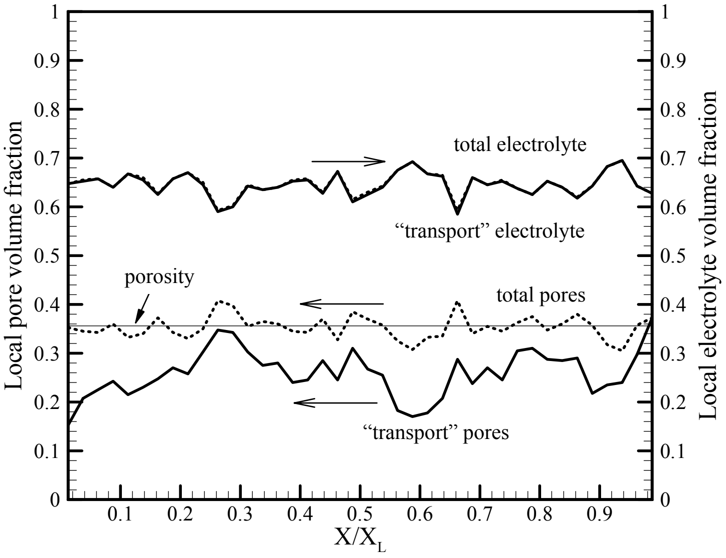

Figure 12. Profiles of pore and electrolyte volume fractions along the thickness of the catalyst layer.

oxygen. On the other hand, near the front end (i.e., adjacent to the right boundary), most of the pores are "transport" pores partly because the structure is open to large pore space in the GDL.

3. Governing Equations

The DNS model developed for the 3-D regular CL microstructure, in the earlier section, is now extended to solve for the conservation equations for charge and oxygen transport on the random 3-D CL structure. The model assumptions remain the same as in the case of the 3-D regular microstructure. The meaning of the symbols can, as well, be traced back correspondingly to the previous sections.

The discrete phase function, *f*, introduced earlier for the regular microstructure, is redefined for each elementary control volume (*i,j,k*) within the entire domain as follows:

$$f(i,j,k) = \begin{cases} 0 & \text{"transport" pores} \\ 1 & \text{"transport" electrolytes} \\ 2 & \text{"dead" pores} \\ 3 & \text{"dead" electrolytes} \end{cases} \tag{31}$$

Correspondingly, the proton conductivity and oxygen diffusivity can be expressed as:

$$K(i,j,k) = \kappa \cdot f(i,j,k) \cdot [2 - f(i,j,k)] \cdot [3 - f(i,j,k)]/2 \tag{32}$$

$$D_{O_2}(i,j,k) = D_{O_2}^{g} \cdot [1 - f(i,j,k)] \cdot [2 - f(i,j,k)] \cdot [3 - f(i,j,k)]/6 \tag{33}$$

For simplicity, we define two new phase functions, f_ϕ and f_{O_2} , as follows:

$$f_\phi(i,j,k) = f(i,j,k) \cdot [2 - f(i,j,k)] \cdot [3 - f(i,j,k)]/2 \tag{34}$$

$$f_{O_2}(i,j,k) = [1 - f(i,j,k)] \cdot [2 - f(i,j,k)] \cdot [3 - f(i,j,k)]/6 \tag{35}$$

Obviously, from the above definitions, it can be seen that f_ϕ is non-zero only within “transport” electrolytes; while f_{O_2} is non-zero only within “transport” pores.

Based on the newly introduced phase functions, Eqs. (32) and (33) can be simplified as:

$$K(i,j,k) = \kappa_e \cdot f_\phi(i,j,k) \tag{36}$$

$$D_{O_2}(i,j,k) = D_{O_2}^{g} \cdot f_{O_2}(i,j,k) \tag{37}$$

The above expressions indicate that both proton conductivity and oxygen diffusivity are set to be zero in “dead” pores and “dead” electrolytes. Now the governing differential equations for charge and oxygen transport, as detailed in the previous section, can be readily extended to be valid in the entire domain using the discrete phase function, *f*(*i*,*j*,*k*). Since the electrochemical reaction only occurs at active phase interfaces, only those “transport” pores and "transport" electrolytes next to each other have source terms, S_{O_2} and S_ϕ respectively. These source terms can be expressed in discretized form as:

$$\begin{aligned} S_\phi(i,j,k) = -\frac{i_0}{c^g_{O_2,ref}} f(i,j,k)\exp[\frac{\alpha_c F}{RT}\phi_e(i,j,k)]\cdot \\ \{[1-f(i-1,j,k)]c_{O_2}(i-1,j,k)/\Delta x \\ +[1-f(i+1,j,k)]c_{O_2}(i+1,j,k)/\Delta x \\ +[1-f(i,j-1,k)]c_{O_2}(i,j-1,k)/\Delta y \\ +[1-f(i,j+1,k)]c_{O_2}(i,j+1,k)/\Delta y \\ +[1-f(i,j,k-1)]c_{O_2}(i,j,k-1)/\Delta z \\ +[1-f(i,j,k+1)]c_{O_2}(i,j,k+1)/\Delta z\} \end{aligned} \tag{38}$$

$$\begin{aligned} S_{O_2}(i,j,k) = -\frac{i_0}{4Fc^g_{O_2,ref}}[1-f(i,j,k)]c_{O_2}(i,j,k)\cdot \\ \{f(i-1,j,k)\exp[\frac{\alpha_c F}{RT}\phi_e(i-1,j,k)]/\Delta x \\ +f(i+1,j,k)\exp[\frac{\alpha_c F}{RT}\phi_e(i+1,j,k)]/\Delta x \\ +f(i,j-1,k)\exp[\frac{\alpha_c F}{RT}\phi_e(i,j-1,k)]/\Delta y \\ +f(i,j+1,k)\exp[\frac{\alpha_c F}{RT}\phi_e(i,j+1,k)]/\Delta y \\ +f(i,j,k-1)\exp[\frac{\alpha_c F}{RT}\phi_e(i,j,k-1)]/\Delta z \\ +f(i,j,k+1)\exp[\frac{\alpha_c F}{RT}\phi_e(i,j,k+1)]/\Delta z\} \end{aligned} \tag{39}$$

Effective proton conductivity is employed since the simulated electrolyte phase also includes the electronic phase as assumed. Similar to the treatment in the earlier sections, a Bruggeman correction is applied:

$$\kappa = \kappa_0 \cdot (\frac{\varepsilon_e}{\varepsilon_e + \varepsilon_s})^{1.5} = \kappa_0 \cdot (\frac{\varepsilon_e}{1-\varepsilon_g})^{1.5} \tag{40}$$

where, ε_e, ε_s and ε_g are the volume fractions of the electrolyte, electronic and gas phases respectively. The intrinsic ionic conductivity, κ_0, is considered to be constant in the present simulations as the membrane is assumed to be fully hydrated.

4. Boundary Conditions

The boundary conditions used for the DNS simulation on random structure remain the same as those described for the regular structure except for the oxygen concentration, $c_{O_2,0}$, at the CL-GDL interface. In the previous simulations, oxygen mass transport resistance through the GDL was ignored and the oxygen concentration at the gas channel inlet was applied directly at the right boundary (CL-GDL interface) of the catalyst layer. In this section, the oxygen concentration drop across the GDL is further included in order to provide a more realistic boundary condition.

As shown schematically in Figure 13, the oxygen concentration in the gas channel is assumed to be uniform, which is physically corresponding to a large stoichiometric flow rate. Through the GDL, an effective diffusion coefficient $D_{O_2,GDL}^{g,eff}$ is applied and the oxygen flux at the CL-GDL interface can be written as:

$$N_{O_2} = D_{O_2,GDL}^{g,eff} \cdot \frac{(c_{O_2,inlet} - c_{O_2,0})}{\Delta X_{GDL}} \tag{41}$$

where, ΔX_{GDL} represents the thickness of the GDL. The porosity ε_{GDL} and tortuosity τ_{GDL} are employed to obtain the effective diffusivity, given as follows:

$$D_{O_2,GDL}^{g,eff} = D_{O_2}^{g} \cdot \frac{\varepsilon_{GDL}}{\tau_{GDL}} \tag{42}$$

$D_{O_2}^{g}$ is the oxygen diffusivity which in turn depends on the specified pressure and temperature[19] as:

$$D_{O_2}^{g} = D_{O_2,0}^{g} \left(\frac{T}{T_0}\right)^{3/2} \left(\frac{p_0}{p}\right) \tag{43}$$

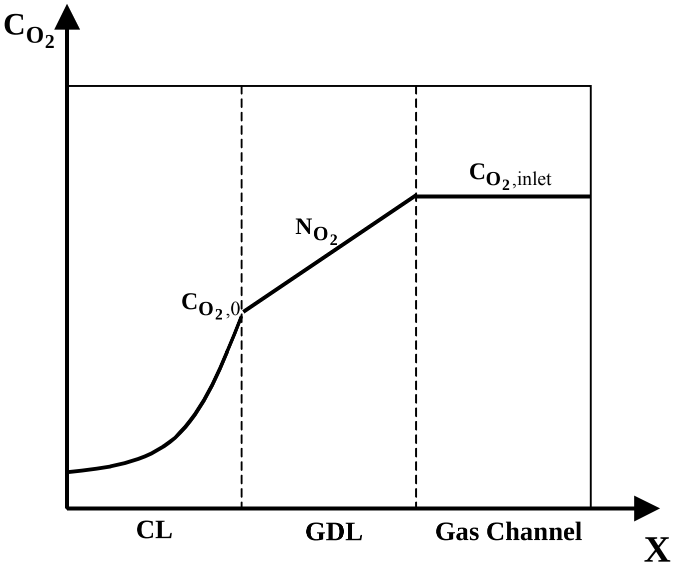

Figure 13. Schematic diagram of the oxygen concentration profile in the cathode.

where, T_0 and p_0 are the reference temperature and pressure respectively; $D^g_{O_2,0}$ is the oxygen diffusivity at the reference condition, T is the fuel cell operating temperature and p is the cathode side inlet gas feed pressure.

At steady state, the total flux through the GDL should be equivalent to the oxygen consumption rate at the catalyst layer, that is:

$$N_{O_2} = \frac{I}{4F} \tag{44}$$

Thus, the oxygen concentration at the CL-GDL interface can be derived by combining Eqs. (41) and (44) and is given by:

$$c_{O_2,0} = c_{O_2,inlet} - \frac{I \cdot \Delta X_{GDL}}{4F \cdot D^{g,eff}_{O_2,GDL}} \tag{45}$$

It is evident that the corrected oxygen concentration depends not only on the inlet oxygen concentration but also on the concentration drop through the GDL. At large operating current densities, there could be a considerable drop across the GDL due to the large oxygen flux.

The model input parameters including the properties of the GDL are summarized in Table 2.

5. Results and Discussion

One of the advantages of constructing the random microstructure is that it provides the phase interfacial area and tortuosity that are comparable with the real catalyst layer microstructures. Hence, using this realistic computer-generated random structure, we can evaluate the Bruggeman correlation required for the macro-homogeneous models using the DNS data. Bruggeman exponent factor ξ is commonly applied to determine the effective property as follows:

$$\Gamma_k^{eff} = \Gamma_k \cdot {\varepsilon_k}^{\xi} \tag{46}$$

In the 1-D macrohomogeneous model, the same specific surface area a (cm^2/cm^3) as that in the constructed random structure is used in the Butler-Volmer equation to represent the volumetric reaction current, that is

Table 2
Property Data for the DNS Calculations with the 3-D Random Microstructure

Parameter	Value
Oxygen diffusivity in gas phase, $D_{O_2}^g$ (m^2/s)	1.9×10^{-5}
Water vapor diffusivity in gas phase, $D_{H_2O}^g$ (m^2/s)	2.6×10^{-5}
Pressure at the gas channel inlet, p (kPa)	150
Operating temperature, T (°C)	80
GDL thickness, ΔX_{GDL} (μm)	300
GDL porosity, ε_{GDL}	0.4
GDL tortuosity, τ_{GDL}	4
Natural porosity of the catalyst layer, ε_g	0.36
Electrolyte volume fraction in the catalyst layer, ε_e	0.3

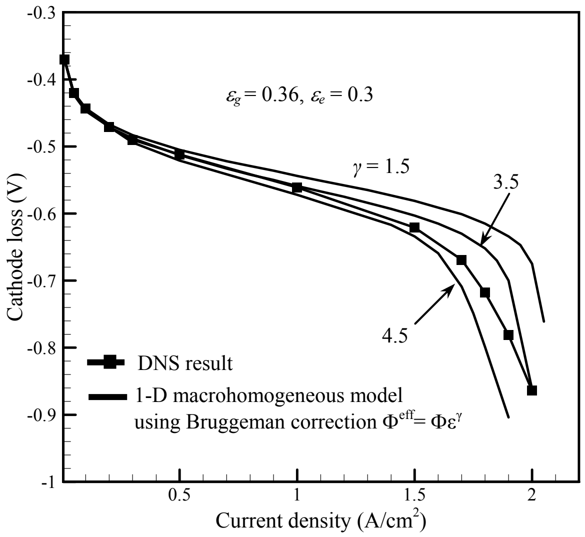

Figure 14. Comparison between the polarization curves from the DNS calculation and the 1-D macrohomogeneous model.

$$j = a \cdot i_0 \left[\exp\left(\frac{\alpha_a F}{RT} \eta \right) - \exp\left(-\frac{\alpha_c F}{RT} \eta \right) \right] \text{ (A/cm}^3\text{)} \qquad (47)$$

The comparison of polarization curves predicted by DNS and 1-D macrohomogeneous models is shown in Figure 14. Three different Bruggeman factors, 1.5, 3.5 and 4.5 were attempted. It can be seen that at small current densities (up to 1 A/cm^2), a factor of 3.5 gives a good match to the DNS model; while in the large current density regime, the Bruggeman factor is suggested to be between 3.5 and 4.5. More elaborate comparisons at the current density of 1.5 A/cm^2, such as the oxygen concentration distribution, cathode overpotential and local reaction current distributions are depicted in Figures 15, 16 and 17 respectively.

In the case of the oxygen concentration (Figure 15), the DNS result is in good agreement with the 1-D macrohomogeneous model with the Bruggeman factor of 4.5. However, Figure 16 shows the factor of 3.5 gives a better match for the shape of the overpotential curve except that the DNS result is about 12 mV higher consistently. The higher surface overpotential stems from the lower active interfacial area in the DNS model. It can be seen from Figure 11 that there are only about 65% of the total interfacial area that is active for the electrochemical reaction. Combination of the findings from Figure 15 and Figure 16 shows that the phase with low volume fraction, i.e., the gas phase in the present study, prefers a higher Bruggeman factor not only because of less tortuosity but also because of a lower effective porosity than the natural porosity. If using the effective porosity of 0.26 in the Bruggeman correlation instead of the natural porosity 0.36, the Bruggeman factor would be about 3.4 (i.e., $0.26^{3.4} \approx 0.36^{4.5}$), very close to that (3.5) for the electrolyte phase. Another point worth noting is that the constructed 3-D microstructure stresses the influence of local variation in the effective porosity on the reaction current distribution; while the macrohomogeneous model only uses a constant natural porosity. As shown in Figure 17, the DNS model generates a more uniform reaction distribution than those of macrohomogeneous models using both Bruggeman factors of 3.5 and 4.5. As displayed in Figure 12, although the natural pore volume fraction of this porous medium distributes uniformly around the average porosity, the effective porosity varies across the

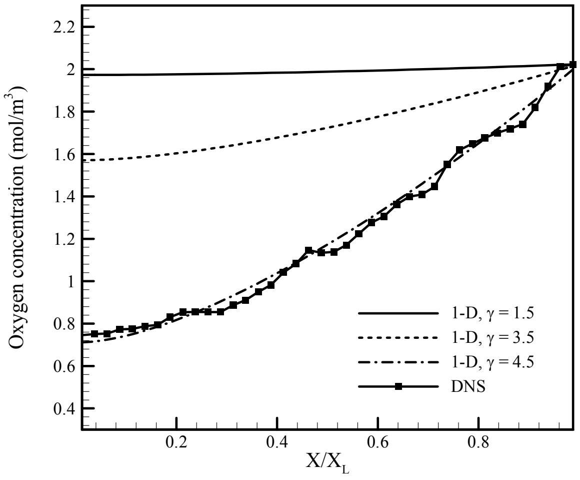

Figure15. Comparison between the cross-sectional averaged oxygen concentration profiles from the DNS and 1-D macrohomogeneous model predictions.

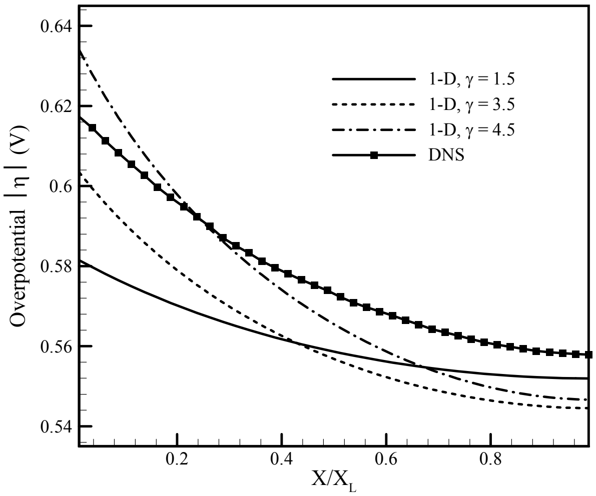

Figure 16. Comparison between the cross-sectional averaged overpotential profiles from the DNS and 1-D macrohomogeneous model predictions.

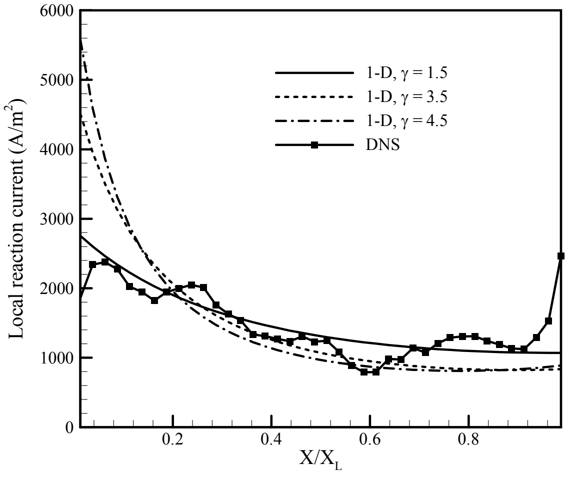

Figure 17. Comparison between the cross-sectional averaged reaction current distributions across the thickness of the catalyst layer from the DNS and 1-D macrohomogeneous model predictions.

thickness of the catalyst layer. More “transport” pores at the front end than at the back end produces a unique reaction current distribution that cannot be captured by the macrohomogeneous model using any Bruggeman correction factor.

IV. DNS MODEL – WATER TRANSPORT

Water management is a central issue in PEFCs. It is referred to as balancing two conflicting requirements: hydration of the polymer electrolyte membrane and avoidance of flooding in porous electrodes and GDL for reactant/product transport. Water management is also a key to high performance and longevity of the polymer membrane. This is because currently available membranes such as Nafion® require water in order to exhibit good proton conductivity. If water is insufficient, the ionomer becomes dehydrated and the proton transport resistance would dramatically increase. On the other hand, liquid water tends to accumulate inside the cathode catalyst layer due to water being produced from the ORR and also water migrating from the anode side via electro-osmotic drag. If water is not removed sufficiently, cathode flooding may occur, resulting in the gas pores being filled with the condensed liquid water, which, in turn, hampers the oxygen diffusion to reaction sites. Generally, fuel and oxidant feed streams are humidified externally to provide adequate water to the polymer membrane. To avoid either membrane dehydration or cathode flooding, it is of great importance to investigate the effect of the inlet humidity on water distribution throughout a cell, particularly inside the cathode catalyst layer, which consists of both the ionomer and gas pores.

Several groups have modeled water transport in PEFCs at various levels of complexity in recent years. Various water transport models for the catalyst layer have been employed in the general framework of computational fuel cell dynamics (CFCD). Notable works include Wang and co-workers,[5,20] Dutta et al.,[21,22] Berning et al.,[23] and Mazumder and Cole.[24] In their work, Dutta et al.[21,22] used an approximate analytical solution for water transport through the membrane. However, they did not consider the MEA in the computational domain. The model of Berning et al.[23] treated the catalyst layer as an interface between the membrane and the GDL. While Mazumder and Cole[24] supposedly ignored any water transport through the membrane, Wang and co-workers,[5,20] in contrast, developed a comprehensive water-transport model applicable throughout a PEFC including the MEA. A recent overview of the various water transport models for a PEFC is provided by Wang.[9] However, all the aforementioned works are based on the macroscopic description. No model has been attempted at the pore-level for water distribution and its intimate interactions with proton transport within the cathode catalyst layer.

In this section, the 3-D DNS model is further extended to include water transport in the cathode catalyst layer. In the previous sections, the proton conductivity of the electrolyte phase was taken to be constant assuming the ionomer to be fully humidified. In the present water transport model, the net water flux through the membrane from the anode side is considered to account for the combined effects of the electro-osmotic drag and back diffusion. Implementation of the various modes of water transport in the DNS model with the 3-D random CL microstructure, generated in the previous section, is described. The effects of humidity and microstructure composition on the cathode performance are investigated in the present section. The importance of the DNS model to optimize the catalyst layer composition is also demonstrated.

1. Water Transport Mechanism

General features of water transport through a PEFC are explained in Figure 18, where a MEA is sandwiched between two gas diffusion layers on the anode and cathode, respectively. To ensure membrane hydration, water is delivered to the fuel cell via humidified fuel and oxidant streams from an external humidifier. Water is transported to the cathode CL from the anode through the membrane by the electro-osmotic drag, expressed by:

$$N_{w,drag} = n_d N_{H^+} = n_d \cdot \frac{I}{F} \tag{48}$$

where, the electro-osmotic drag coefficient, n_d, denotes the number of water molecules carried by each proton across the membrane as current is passed and N_{H^+} is the proton flux. n_d varies in a wide range depending on the degree of membrane hydration according to the experimental measurements by Zawodzinski et al.[25] For a fully hydrated membrane immersed in liquid water, 2.5 water molecules are dragged per H^+ transported, while for a partially hydrated membrane corresponding to the water content up to 14, the drag coefficient is relatively constant at 1.0. In the present

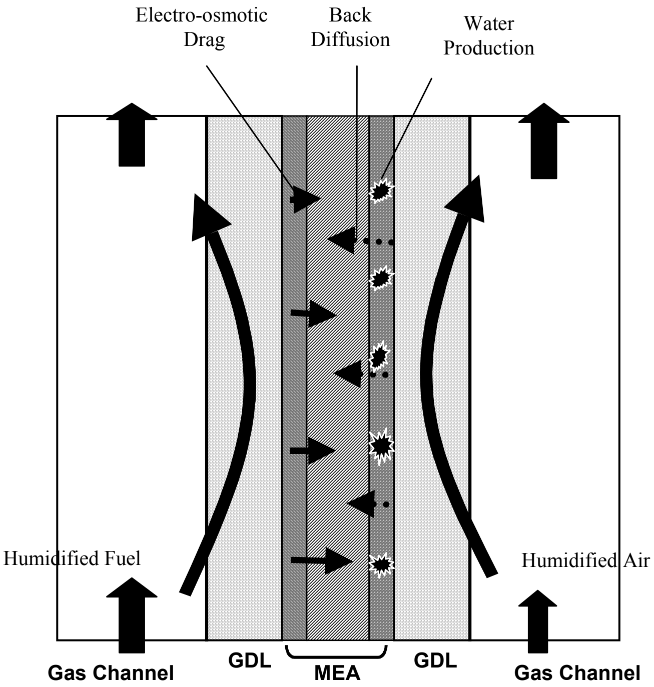

Figure 18. Schematic diagram of the water transport and distribution in a PEFC.

study, a constant drag coefficient of unity is used because the water content of interest ranges from zero to 14.

On the cathode side, water is generated by the ORR. The increase of water concentration from production will result in the back diffusion of water to the anode across the membrane. The back diffusion helps to hydrate the membrane on the anode side and thus partly compensates for the water loss by electro-osmotic drag. At higher current densities, the excessive water produced at the cathode is removed via evaporation by the under-saturated oxidant stream, and the removal rate can be controlled by adjusting the inlet air humidity and flow rate through the flow field.

2. Mathematical Description

Based on the DNS model described in the previous sections, the following assumptions are additionally made for the modeling of water transport:

- water is in the gas phase even if the water vapor concentration slightly exceeds the saturated value (i.e., slight over-saturation is allowed);
- equilibrium between the water in the electrolyte phase and in the gas phase is assumed and hence it is sufficient to consider water transport only through the gas phase;
- the electro-osmotic drag coefficient is constant at unity; and
- the net water transport coefficient from the anode to cathode is assumed constant.

Figure 19 describes various water transport mechanisms in both gas and electrolyte phases through the catalyst layer that are included in the present DNS model. Similar to the oxygen transport equation described earlier, the conservation equation for water vapor concentration, c_{H_2O} , through the random catalyst layer microstructure, generated in Section III, can be expressed as:

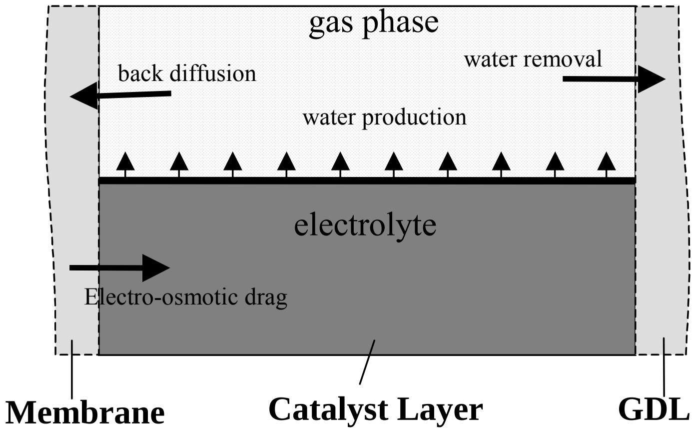

Figure 19. Schematic diagram of the water transport mechanisms inclued in the DNS model.

$$\nabla\cdot(D^g_{H_2O}\nabla c_{H_2O})+a\int_\Gamma\frac{j}{2F}\delta(x-x_{interface})ds=0 \tag{49}$$

where, $D^g_{H_2O}$ is the diffusion coefficient of water in the gas phase and definitions of the rest of the symbols remain the same as described earlier. Now, adopting the single-domain approach as detailed earlier, the water vapor diffusivity and source term in Eq. (49) can be expressed in terms of the discrete phase function, *f(i,j,k)*, respectively, as:

$$\begin{aligned}D_{H_2O}(i,j,k)=&\\ &D^g_{H_2O}\cdot[1-f(i,j,k)]\cdot[2-f(i,j,k)]\cdot[3-f(i,j,k)]/6\end{aligned} \tag{50}$$

$$\begin{aligned}S_{H_2O}(i,j,k)=\frac{i_0}{2Fc^g_{H_2O,ref}}&[1-f(i,j,k)]c_{H_2O}(i,j,k)\cdot\\ &\{f(i-1,j,k)\exp[\frac{\alpha_cF}{RT}\phi_e(i-1,j,k)]/\Delta x\\ &+f(i+1,j,k)\exp[\frac{\alpha_cF}{RT}\phi_e(i+1,j,k)]/\Delta x\\ &+f(i,j-1,k)\exp[\frac{\alpha_cF}{RT}\phi_e(i,j-1,k)]/\Delta y\\ &+f(i,j+1,k)\exp[\frac{\alpha_cF}{RT}\phi_e(i,j+1,k)]/\Delta y\\ &+f(i,j,k-1)\exp[\frac{\alpha_cF}{RT}\phi_e(i,j,k-1)]/\Delta z\\ &+f(i,j,k+1)\exp[\frac{\alpha_cF}{RT}\phi_e(i,j,k+1)]/\Delta z\}\end{aligned} \tag{51}$$

The water vapor diffusivity, $D^g_{H_2O}$, also depends on the temperature and pressure similar to the treatment of oxygen diffusivity as described by Eq. (41) and $D^g_{H_2O,0}$ is the reference water vapor diffusivity in the gas phase. The proton conductivity in the electrolyte phase has been correlated by Springer et al.[26] from the experiments as:

$$\kappa_0(\lambda)=100\exp[1268(\frac{1}{303}-\frac{1}{T})](0.005139\lambda-0.00326)\quad \text{S/m} \tag{52}$$

where, the water content in the membrane, λ , depends on the water activity, a, in the gas phase according to the following fit of the experimental data:

$$\lambda = \begin{cases} 0.043 + 17.81a - 39.85a^2 + 36.0a^3 & for \quad 0 < a \le 1 \\ 14 + 1.4(a-1) & for \quad 1 < a \le 3 \end{cases} \tag{53}$$

The water activity, a, is defined as:

$$a = \frac{c_{H_2O}}{c_{H_2O}^{sat}} \tag{54}$$

where, $c_{H_2O}^{sat}$ is the saturation concentration of water vapor corresponding to the fuel cell operating temperature. The saturation pressure of water vapor is only a function of temperature, which has been formulated by Springer et al.[26] as follows:

$$\begin{aligned} \log_{10} p^{sat} &= -2.1794 + 0.02953(T - 273.15) \\ &\quad - 9.1837 \times 10^{-5} (T - 273.115)^2 \\ &\quad + 1.4454 \times 10^{-7} (T - 273.15)^3 \end{aligned} \tag{55}$$

where the pressure is in bar. Substitution of Eq. (53) into Eq. (52) provides the dependence of proton conductivity on water activity. Thus a water concentration distribution will cause the proton conductivity of the electrolyte phase to vary at every point within the catalyst layer.

Similar to the boundary conditions for charge and oxygen transport, a symmetry boundary condition is applied for the water conservation equation in y and z directions of the computational domain. At the CL-membrane interface, a net water transport coefficient, α, is employed to account for the net water flux across the membrane. It combines the electro-osmotic drag and back diffusion effects, and can be expressed as:

$$N_{w,net} = \alpha \cdot \frac{I}{F} = N_{w,drag} - N_{w,dif} \tag{56}$$

where, $N_{w,dif}$ is the water flux through the membrane due to back diffusion from the cathode side to the anode side. In the present study, α is assumed to be constant although it depends on the reaction rate and humidity conditions at anode and cathode inlets. Thus the boundary condition at the CL-membrane interface is given by

$$\frac{\partial c_{H_2O}}{\partial x}\Big|_{x=x_L} = -N_{w,net} / D^g_{H_2O} \tag{57}$$

At the boundary connected to the GDL, i.e., at the CL-GDL interface, the water vapor concentration can be calculated from the water concentration at the channel inlet, $c_{H_2O,inlet}$, after the mass transport resistance through the GDL is accounted for and is given by:

$$c_{H_2O}\Big|_{x=x_L} = c_{H_2O,inlet} + N_w\Big|_{x=x_L} \cdot \frac{\Delta X_{GDL}}{D^{g,eff}_{H_2O,GDL}} \tag{58}$$

The water vapor profile is assumed to be linear across the GDL. The water flux through the GDL is the sum of the net flux across the membrane and the water production rate in the catalyst layer, $N_{w,prod}$, and can be expressed as:

$$N_w\Big|_{x=x_L} = N_{w,net} + N_{w,prod} = (\alpha + 0.5) \cdot \frac{I}{F} \tag{59}$$

In Eq. (58), the inlet water concentration, $c_{H_2O,inlet}$, is calculated from the inlet air humidity and fuel cell operating pressure and temperature. Similar to the treatment in Section III, the water transport in the gas channel is assumed constant, which corresponds to a relatively large stoichiometric flow rate. From the inlet relative humidity, represented by *RH*, water vapor concentration of the humidified air is calculated by:

$$c_{H_2O,inlet} = RH \cdot c^{sat}_{H_2O} \tag{60}$$

All the parameters used in this section remain the same as those summarized in Table 2 in Section III.

3. Results and Discussion

(*i*) *Inlet-Air Humidity Effect*

Fuel/oxidant inlet humidity designs play an important role in the balance of water production and removal. Without a proper control, imbalance of water may result in either dehydration of the polymer membrane or flooding of the air cathode. Low-humidity is always desirable from the standpoint of external humidifiers with reduced size and cost.

Figure 20 displays several polarization curves of the cathode for the relative humidity ranging from 5% to 100%. There are three distinct characteristics corresponding to the three different regimes, kinetic control regime, ohmic control regime, and mass transport control regime, respectively. First, within the kinetic regime, the cathode performance is about the same and the only loss is kinetic activation loss. The only factor influencing the kinetic loss among these three cases is the oxygen concentration inside the catalyst layer. Calculations show that the oxygen concentrations are 7.5 mol/m^3, 9.2 mol/m^3 and 10.7mol/m^3 for 100%, 50%, and 5% inlet

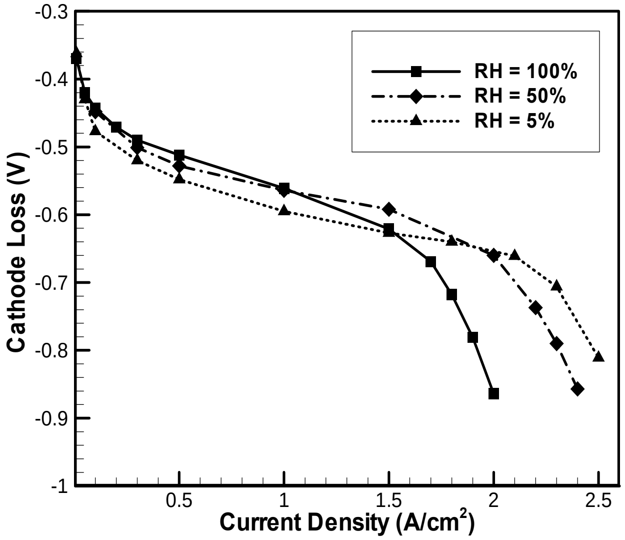

Figure 20. Polarization curves for various inlet humidity.

air humidity, respectively. These differences only bring about minor variations to the kinetic loss. According to the Tafel slope of 70 mV/dec, the case with 100% air humidity has 10 mV more kinetic loss than that with 5% relative humidity.

Secondly, low humidity tends to extend the ohmic control regime, postponing the occurrence of the mass transport limitation. This is the salient advantage of low-humidity operation. At 100% humidity, the oxygen concentration near the membrane end is as low as 0.2 mol/m^3 and the region is about to be depleted of oxygen. From the polarization curve, it can also be seen that the curve begins to fall off at the current density greater than 1.5 A/cm^2.

Thirdly, the disadvantage of low-humidity operation is its larger voltage loss in the ohmic control regime though the regime itself is enlarged. This is because of the low proton conductivity associated with partially hydrated electrolyte phase, leading to the increased ohmic loss. Figure 21 shows that the reaction zone shifts towards the back end of the catalyst layer (close to the membrane) with lowering of the inlet humidity. Apparently, this is due to

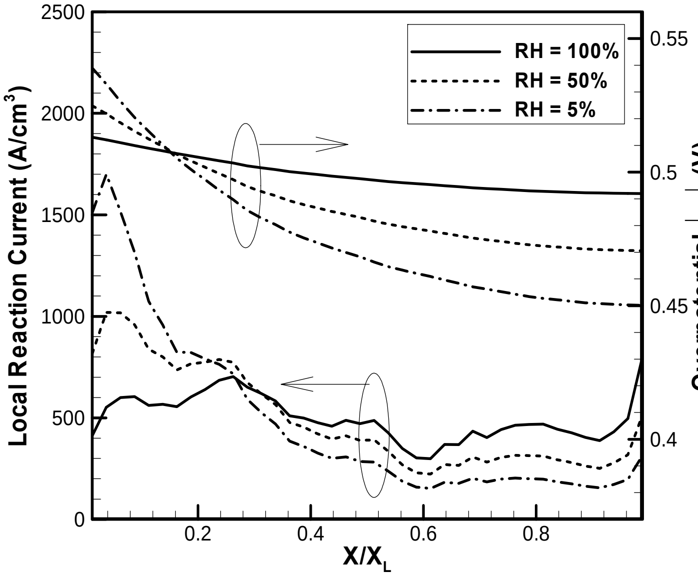

Figure 21. Overpotential and reaction current distributions for different inlet humidity.

poorer proton conductivity or higher ohmic resistance in the electrolyte phase and results in a much lower surface overpotential at the front end of the catalyst layer, making the overpotential distribution more nonuniform. In order to compensate for lower reaction current produced near the front end of the catalyst layer, the back end must provide higher reaction current as the average current density is fixed. This leads to a higher surface overpotential needed at the back end of the layer, representing more total voltage loss of the cathode in the low-humidity case.

In summary, 50% appears to be the optimal relative humidity in the catalyst layer configuration modeled here. It has a large range of ohmic control at a minimum expense of kinetic loss. It should be noticed that since the present model only considers the water transport in the gas phase, another significant advantage of low-humidity operation to alleviate cathode flooding cannot be demonstrated although it is widely recognized in practical applications.

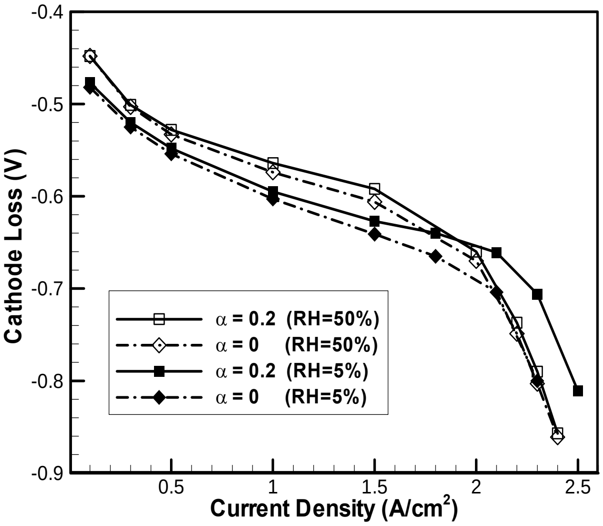

Figure 22. Polarization curves with different net water transport coefficients at the inlet humidity of 50% and 5%.

(*ii) Water Crossover Effect*

In the present DNS model, the net water flux through the polymer membrane to the cathode catalyst layer is quantified by the net water transport coefficient as given by Eq. (57). The value of this coefficient reflects the contribution of water transferred from the anode to the cathode. It depends on the humidity condition on the anode side. Low value of α indicates strong back diffusion from the cathode, which means a relatively dry condition in the anode. When α is close to its highest value, 1.0, it means the water flux due to electro-osmotic drag is dominant and the back diffusion is negligible. Therefore, by studying the effect of the net water transport coefficient, we can understand how important the anode gas humidification is to the cathode catalyst layer performance.

Two cases of the net water transport coefficient, 0.2, and 0, are studied under two different cathode inlet humidities, i.e., 50% and 5%. The polarization curves of the cathode are plotted in Figure 22 for all the four operating conditions. First, it shows that under 50% cathode inlet humidity, the value of α has almost no influence on the cathode voltage loss. The greatest difference of about 15 mV occurs at 1.5 A/cm^2. At operating current densities greater than 1.5 A/cm^2, the cathode performance almost has no change, which indicates the cathode side is already humid enough due to the large water production rate even if there is no water transported from the anode. However, with the cathode inlet humidity of 5%, α value becomes important especially at large current densities. The possible explanation is that the cathode is largely dry and hence any water supply from the anode is very helpful for increasing the proton conductivity of the electrolyte.

In summary, The DNS results clearly show that at 5% RH there is a considerable increase in the cathode voltage loss as α is reduced to zero. Again, this is due to the lower water activity, leading to the lower proton conductivity of the electrolyte phase. The lower proton conductivity would push the reaction zone to the back end, consuming more oxygen there. The larger consumption rate of oxygen, in turn, reduces the oxygen concentration there, which eventually requires a larger overpotential to drive the reaction. This series of consequences leads to the total cathode voltage loss to increase greatly with α being zero. The parametric study clearly suggests that at low cathode inlet humidity, restraining the back diffusion of water to the anode side is important and can significantly improve the cathode performance with better-hydrated electrolyte phase.

(*iii*) *Optimization of Catalyst Layer Compositions*

Besides the inlet humidity and water transport effects on the cathode performance, optimal design of the catalyst layer compositions is also of great practical interest. A series of simulations for various combinations of pore and electrolyte volume fractions were carried out to investigate the electrode composition effect. The predicted polarization curves under different compositions of pore and electrolyte phases are displayed in Figure 23. It can be seen that the greater the porosity, the larger the mass transport limiting current density. This is quite straightforward, as the oxygen transport would benefit from a large number of pores.

Figure 24 shows the local reaction current and overpotential distributions at a current density of 0.5 A/cm^2. With the porosity of 0.34 and electrolyte volume fraction of 0.32, the resulting small amount of "transport" pores limits the back end of the catalyst layer being accessed by oxygen. The increasing loss is then due to the ionic current passing through the back part of the catalyst layer without reaction (the resistance is much lower to pass current through the electronic phase after charge transfer reaction). As the porosity is increased, between 0.36 and 0.4, there is only a slight difference, which is due to the larger reaction sites of porosity 0.4. At the porosity of 0.6, Figure 24 shows that most of the reaction is concentrated at the back end, an indication that the proton conductivity is very poor. This is obviously because the electrolyte fraction has been reduced to 0.2 (the mixed electrolyte/electronic phases occupy (1-ε_g)), a typical design of the catalyst layer.

In summary, by assuming a sufficiently large electronic conductivity of the Pt/C phase and a fixed electronic phase volume fraction, it is important to select an appropriate pore to electrolyte volume ratio in order to achieve the best performance of the cathode. In general, both the pore and electrolyte volume fractions should be larger than the percolation threshold. Under this prerequisite, further increasing the porosity and electrolyte volume fraction will relax the mass transport limitation and reduce the ohmic drop, respectively. Hence, there always exists an optimal composition design for the best trade-off. According to the present simulation results of the DNS model, the optimal compositions are 0.4 for the porosity and 0.26 for the electrolyte volume fraction. In comparison, the traditional design with the electrolyte volume faction of 0.2 gives high ionic resistance. On the other hand, a

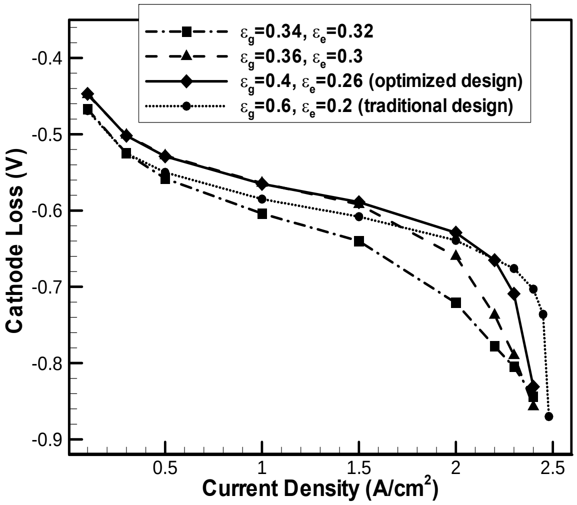

Figure 23. Polarization curves for different combinations of void and electrolyte volume fractions.

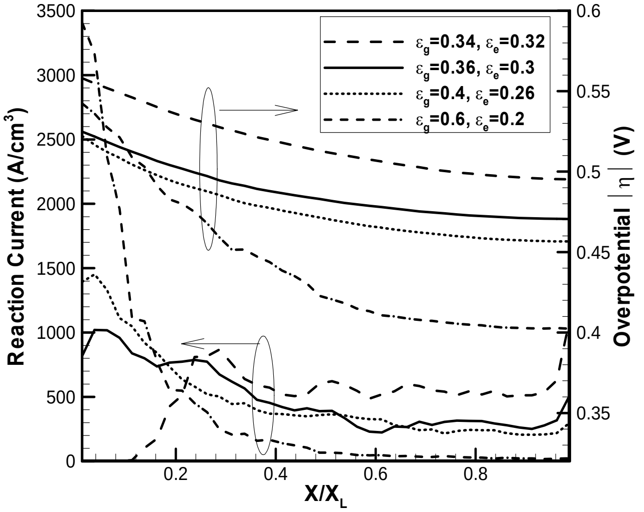

Figure 24. Local reaction current and overpotential distributions at 0.5 A/cm^2 for different combinations of void and electrolyte volume fractions.

relatively large porosity does not benefit the cathode performance much other than slightly delaying the mass transport control regime.

V. 3-D CORRELATED MICROSTRUCTURE

In the Section III, the generated 3-D microstructure only portrays the random nature of the porous media with an arbitrarily chosen porosity. However, the disorder in terms of randomness incorporated into the structure does not directly relate to the statistical inputs from an actual catalyst layer structure. This limitation is circumvented in the present section through the stochastic generation of a 3-D correlated microstructure.

1. Stochastic Generation Method

The process of generating a three-dimensional random porous medium with a given porosity and a given correlation function has been detailed by Adler.[18] The principle of this numerical reconstruction method is composed of two major steps. The first step involves the experimental measurement of any salient geometry features. Different features can be chosen for various materials. In most studies, the porosity and correlation function of pore spaces are selected. For this purpose, a representative portion of a SEM or TEM image of the catalyst layer is digitized to obtain an array of grayscale values for each pixel. Then using a computer program the image is converted into a two-dimensional solid map with artifacts removed by certain filters. Subsequently, statistical data such as correlation function and porosity are collected. The second step is the reconstruction process. Random samples of porous media are generated in such a way that, on average, they possess the same statistical properties as the real samples that they are assumed to mimic. Once these samples are generated, all transport processes can be studied at least in principle. For example, in the DNS model, using the phase function, a single set of governing equations can be derived and solved to analyze transport of reactants and product in both phases.

The stochastic method is based on the idea that an arbitrarily complex pore structure can be described by the values of a phase function $Z(\vec{r})$, described by Eq. (28) at each point $\vec{r}$ in the porous medium. For a statistically homogeneous porous medium, the resulting microstructure can be described fully, albeit implicitly, by the first two moments of the phase function, namely porosity, ε and two-point autocorrelation function, $R_z(\vec{u})$ which are represented by Eqs. (29) and (30) respectively.

In general, the stochastic method creates a realization of the 3-D porous medium in terms of a binary, discrete population *Z(x),* which takes only two-values 0 and 1, by transforming a Gaussian set *X(x)* of standard, normal variates *x*. The final 3-D binary image represents a porous rock of prescribed porosity and autocorrelation function. This statistics-based reconstruction method was originally developed in two-dimensions by Joshi[27] and extended to three dimensions by Quiblier.[28] Adler et al.[29] applied it to the reconstruction of Fontainbleau sandstone. Ioannidis et al.[30] modified this method slightly by using Discrete Fourier Transform. In our study, we employed a simplified version, by Bentz et al.,[31] of the approach outlined by Quiblier.[28] The simplification of this method, over the approach utilized by Quiblier,[28] comes from the fact that there is no need to handle a large system of nonlinear equations in order to compute the matrix of filtering coefficients and this is numerically superior since no inversion is required.

Starting with the 2-D TEM image of an actual catalyst layer, as shown in Figure 25(a), the stochastic reconstruction technique first computes the two-point autocorrelation function from the binarized (pore/solid) 2-D image in Figure 25(b), generated from the original 2-D image in Figure 25(a). Using this correlation function and a nominal porosity of 0.6 as inputs, it finally produces the 3-D correlated microstructure representation of the catalyst layer, as shown in Figure 26, after passing it through the structural designation loop mentioned in Section III, which assigns the corresponding “transport” and “dead” pore and electrolyte phases.

2. Governing Equations, Boundary Conditions and Numerical Procedure

The governing equations for the conservation of charge, oxygen and water vapor remain the same as furnished in the previous sections. The symmetry boundary condition is imposed in the y and z directions of the computational domain, as shown in Figure 26. The rest of the boundary conditions are identical to the ones imposed for the 3-D random CL microstructure, as detailed in Sections III and IV. The conservation equations (16), (17) and (49) were solved using the commercial CFD software Fluent.®[32] The User Defined Functions (UDF) capability was deployed to

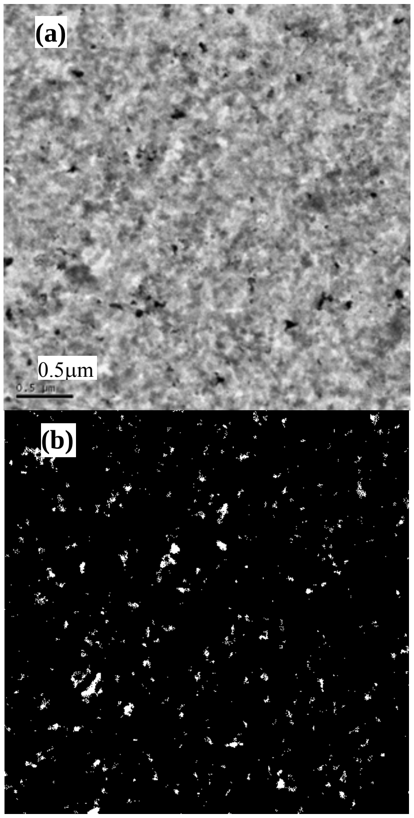

Figure 25. (a) Original 2-D TEM image of the CL, (b) Binary (pore/solid) 2-D image as input to the microstructure reconstruction model.

customize the source terms given by Eqs. (38), (39) and (51) for modeling the electrochemical reactions at the phase interface as well as to solve the set of governing equations for DNS. Convergence was considered achieved when the relative error, for each scalar, between two successive iterations reached 10^{-6}. The same numerical procedure was also employed for the DNS calculations with the regular and random 3-D microstructures in the previous sections. The property data used for the DNS calculations using the correlated microstructure are summarized in Table 3. In the present study for the correlated microstructure, the

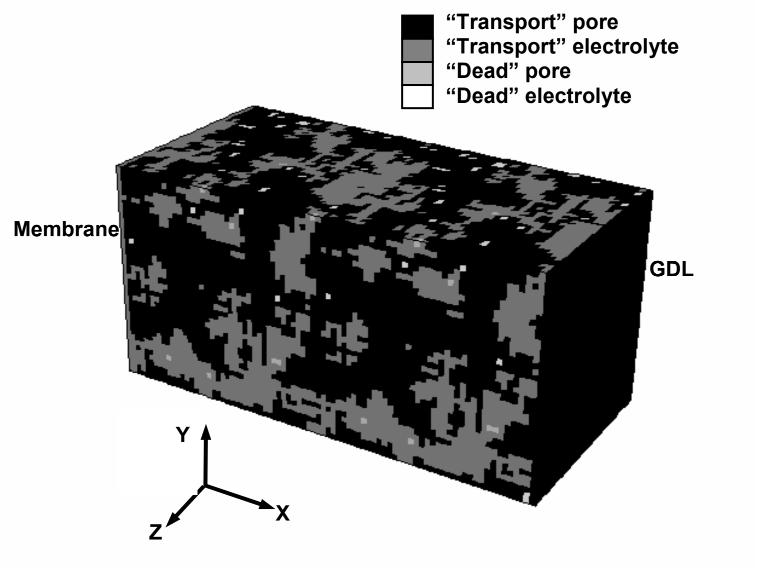

Figure 26. 3-D correlated microstructure of the catalyst layer with nominal porosity of 0.6.

Table 3
Property Data for the DNS Calculations with the 3-D Correlated Microstructure.

Parameter	Value
Oxygen diffusivity in air, $D^g_{O_2}$ (m^2/s)	9.5×10^{-6}
Water vapor diffusivity in air, $D^g_{H_2O}$ (m^2/s)	1.28×10^{-5}
Oxygen diffusivity in helox, $D^g_{O_2}$ (m^2/s)	2.0×10^{-5}
Water vapor diffusivity in helox, $D^g_{H_2O}$ (m^2/s)	3.3×10^{-5}
Pressure at the gas channel inlet, p (kPa)	200
Operating temperature, T (°C)	70
GDL thickness, ΔX_{GDL} (μm)	290
GDL porosity, ε_{GDL}	0.6
GDL tortuosity, τ_{GDL}	1.5
Nominal porosity of catalyst layer, ε_g	0.6

number of cells within the computational domain in the *x*, *y* and *z* directions are 100×50×50, respectively, leading to an average pore size of 0.1 μm and is found to be sufficient.

3. Results and Discussion

Figures 27, 28 and 29 show the comparison of cross-section averaged reaction current, cathode overpotential and oxygen concentration profiles at an average current density of 0.6 A/cm^2 with air as the oxidant along the thickness of the CL between the DNS and 1-D macrohomogeneous models, respectively. Different Bruggeman factors have been attempted. In the case of the reaction current (Figure 27) and cathode overpotential (Figure 28) distributions, the DNS result exhibits good agreement with the 1-D macrohomogeneous model with the Bruggeman factor of 3.5. However, Figure 29 shows that the factor of 4.5 gives a better match for the oxygen concentration profile. This feedback about the Bruggeman factor from the DNS data is very useful and can be used in the full-scale computational fuel cell dynamics (CFCD) models to effectively model the porous media. It is also important to note that the high reaction current in the 15-20% of the region near the membrane, as is evident in Figure 27, could be attributed

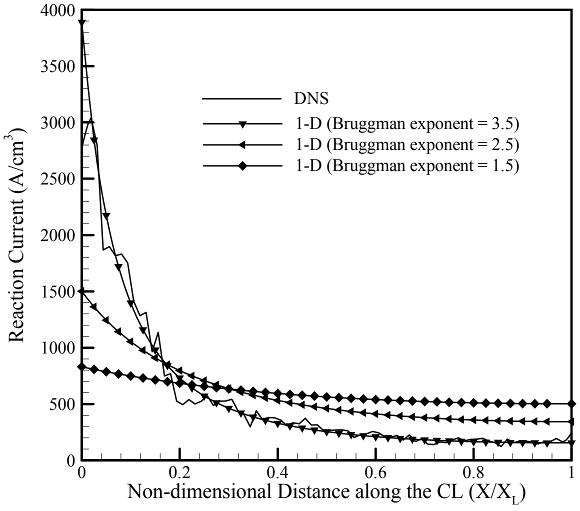

Figure 27. Local reaction current distribution along the thickness of the CL.

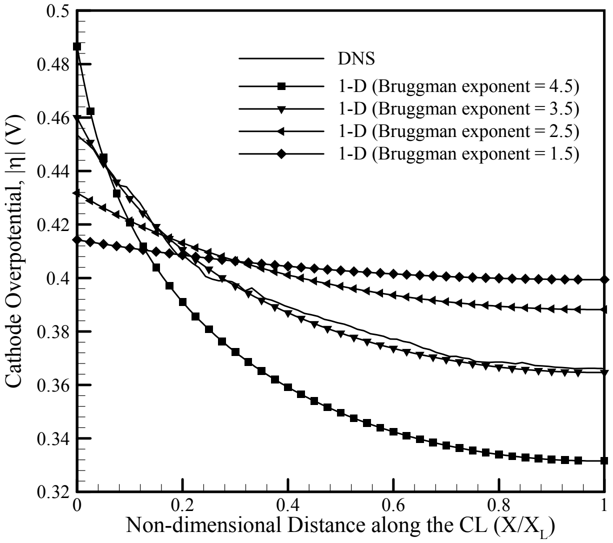

Figure 28. Local cathode overpotential distribution along the thickness of the CL.

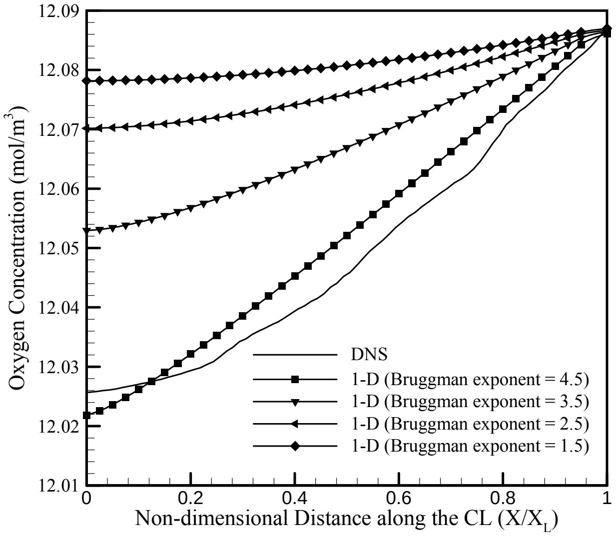

Figure 29.Local oxygen concentration distribution along the thickness of the CL.

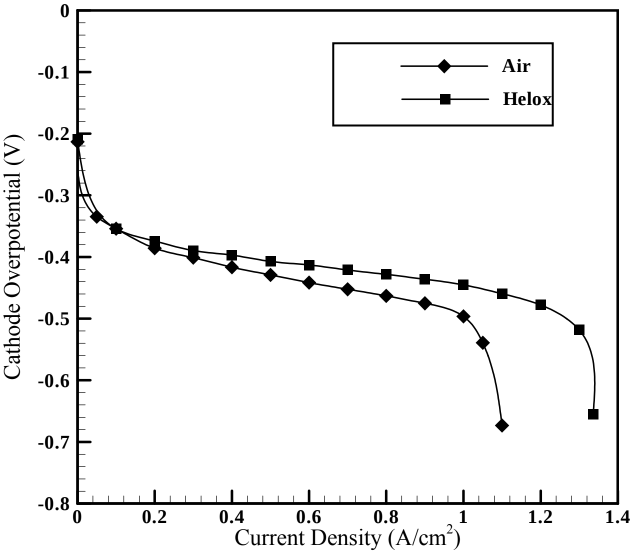

Figure 30. Polarization curves for 100% RH air and helox as oxidants.

to the limited ionomer conductivity resulting from low electrolyte phase volume fraction, estimated to be approximately 11%, which was calculated, based on the method outlined by Gastieger,[17] from the mass loading data of the respective constituent phases i.e., Pt, carbon and Nafion,® used in the recipe for the catalyst layer preparation.

Figure 30 shows the polarization curves with air and helox as oxidants under 100% RH inlet condition. From, Figure 30, it is evident that the cell performance is greatly improved when operated with helox as compared to with air due to the reduction in oxygen transport resistance. Higher performance is expected for helox, since oxygen diffusivity is almost two-times higher in He background (as in helox) as compared to in N_2 background (as in air). Also, as expected, for fully-humidified helox, DNS calculations predict a higher value of the limiting current density than that for fully-humidified air.

VI. CONCLUSIONS

In this chapter, the progress recently made in the pore-scale modeling of the PEFC catalyst layer is described. The DNS method, presented in the chapter, can directly model the transport and electrochemical reactions at the pore level of the catalyst layer with detailed morphology of the electrochemically active surface, ionomer network and pore tortuosity. It, thus, helps to investigate the microstructural influence of electrodes and permit optimization of morphology, composition and operating conditions to achieve high performance. The DNS model also has the capability to allow for virtual assessment of Pt/C ratio, solvents used in catalyst layer fabrication, Nafion® content etc. to maximize catalyst utilization and minimize g Pt/kW. To sum up:

- The DNS model provides a fast screening tool for optimizing catalyst layer compositions and structures.
- It provides an alternative approach to simulate fuel cell catalyst layers that is otherwise difficult to be characterized experimentally.
- It establishes a fundamental database to corroborate empirical correlations for effective parameters used in macroscopic models based on computational fluid dynamics.
- The DNS method establishes a science-based approach instead of Edisonian approach in providing inputs for development of novel recipes for next-generation, high-performance catalyst layers.

ACKNOWLEDGEMENTS

Financial support from NSF and industrial sponsors of ECEC is gratefully acknowledged. PPM wants to express sincere thanks to Mr. D. P. Bentz at National Institute of Standards and Technology (NIST), USA for many fruitful discussions during the stochastic reconstruction model development for the 3-D, correlated microstructure from TEM images, and Dr. X. G. Yang at ECEC for providing the TEM images.

REFERENCES

[1] S. Gottesfeld and T. A. Zawodzinski, in *Advances in Electrochemical Science and Engineering*, Vol. 5, Ed. by C. Tobias, Wiley and Sons, New York, 1997.

[2] T. E. Springer, T. A. Zawodinski, and S. Gottesfeld, *J. Electrochem. Soc.* **138** (1991) 2334.
[3] D. M. Bernardi and M. W. Verbrugge, *J. Electrochem. Soc.* **139** (1992) 2477.
[4] V. Gurau, H. Liu, and S. Kakac, *AIChE J.* **44** (1998) 2410.
[5] S. Um, C. Y. Wang, and K. S. Chen, *J. Electrochem. Soc.* **147** (2000) 4485.
[6] T. E. Springer and S. Gottesfeld, in *Modeling of Batteries and Fuel Cells*, Ed. by R. E. White, Electrochem. Soc. Proc., Pennington, NJ, 1991, p. 197.
[7] M. L. Perry, J. Newman, and E. J. Cairns, *J. Electrochem. Soc.* **145** (1998) 5.
[8] M. Eikerling and A. A. Kornyshev, *J. Electroanal. Chem.* **453** (1998) 89.
[9] C. Y. Wang, *Chem. Rev.* **104** (2004) 4727.
[10] A. Z. Weber and J. Newman, *Chem. Rev.* **104** (2004) 4679.
[11] L. Pisani, M. Valentini, and G. Murgia, *J. Electrochem. Soc.* **150** (2003) A1558.
[12] G. Wang, PhD Dissertation, Deptartment of Mechanical and Nuclear Engineering, The Pennsylvania State University (2003).
[13] J. Stumper, H. Haas, and A. Granados, *J. Electrochem. Soc.* **152** (2005) A837.
[14] T. Baritaud, T. Poinsot and M. Baum, *Direct Numerical Simulation for Turbulent Flows*, Publisher, Paris. Ed. Technip (1996).
[15] M. Sahraoui and M. Kaviany, *Int. J. Heat Mass Transfer* **37** (1994) 2817.
[16] S. V. Patankar, *Numerical Heat Transfer and Fluid Flow*, Hemisphere, Washington DC (1980).
[17] H. A. Gasteiger, W. Gu, R. Makharia, M. F. Mathias, and B. Sompalli, in *Handbook of Fuel Cells—Fundamentals, Technology and Applications*, Vol. 3, Ed. by W. Vielstich, A. Lamm, and H. A. Gasteiger, Wiley, Chichester, 2003, Ch. 46.
[18] P. M. Adler, *Porous Media: geometry and transports*, Butterworth-Heinemann, Stoneham, MA (1992).
[19] R. B. Bird, W. E. Stewart, and E. N. Lightfoot, *Transport Phenomena*, John Wiley & Sons Inc., New York (1960).
[20] S. Um, and C. Y. Wang, *J. Power Sources* **125** (2004) 40.
[21] S. Dutta, S. Shimpalee, and J. W. Van Zee, *J. Appl. Electrochem.* **30** (2000) 135.
[22] S. Dutta, S. Shimpalee, and J. W. Van Zee, *Int. J. Heat Mass Transfer* **44** (2001) 2029.
[23] T. Berning, D. M. Lu, and N. Djilali, *J. Power Sources* **106** (2002) 284.
[24] S. Mazumder and J. V. Cole, *J. Electrochem. Soc.* **150** (2003) A1503.
[25] T. A. Zawodzinski, J. Davey, J. Valerio, and S. Gottesfeld, *Electrochimica Acta*, **40** (1995) 297.
[26] T. E. Springer, T. A. Zawodzinski, and S. Gottesfeld, *J. Electrochem. Soc.* **138** (1991) 2334.
[27] M. Joshi, Ph.D. Dissertation, U. of Kansas, Lawrence, Kansas (1974).
[28] J. A. Quiblier, *J. Coll. Interf. Sci.* **98** (1984) 84.
[29] P. M. Adler, C. G. Jacquin, and J. A. Quiblier, *Int. J. Multiphase Flow* **16** (1990) 691.
[30] M. Ioannidis, M. Kwiecien, and I. Chatzis, *SPE Petroleum Computer Conference*, Houston, 11-14 June (1995).
[31] D. P. Bentz, and N. S. Martys, *Transport in Porous Media* **17** (1995) 221.
[32] Fluent 6.1 UDF Manual, Fluent Inc., NH, USA.